SANDIA REPORT

SAND2017-8056
Unlimited Release
Printed July 2017

Ultra-Low Noise Germanium Neutrino Detection system (ULGeN)

Belkis Cabrera-Palmer
Paul Barton

Prepared by
Sandia National Laboratories
Albuquerque, New Mexico 87185 and Livermore, California 94550

Sandia National Laboratories is a multimission laboratory managed and operated by National Technology and Engineering Solutions of Sandia, LLC, a wholly owned subsidiary of Honeywell International, Inc., for the U.S. Department of Energy's National Nuclear Security Administration under contract DE-NA0003525.

Sandia National Laboratories

Issued by Sandia National Laboratories, operated for the United States Department of Energy by National Technology and Engineering Solutions of Sandia, LLC.

Available to DOE and DOE contractors from

U.S. Department of Energy
Office of Scientific and Technical Information
P.O. Box 62
Oak Ridge, TN 37831

Telephone: (865) 576-8401
Facsimile: (865) 576-5728
E-Mail: reports@osti.gov
Online ordering: http://www.osti.gov/scitech

Available to the public from

U.S. Department of Commerce
National Technical Information Service
5301 Shawnee Rd
Alexandria, VA 22312

Telephone: (800) 553-6847
Facsimile: (703) 605-6900
E-Mail: orders@ntis.gov
Online order: http://www.ntis.gov/search

SAND2017-8056
Unlimited Release
Printed July 2017

Ultra-Low Noise Germanium Neutrino Detection system (ULGeN)

Belkis Cabrera-Palmer
Sandia National Laboratories
P.O. Box 5800
Albuquerque, New Mexico 87185-MSXXXX

Paul Barton
Lawrence Berkeley National Laboratory

Abstract

Monitoring nuclear power plant operation by measuring the antineutrino flux has become an active research field for safeguards and non-proliferation. We describe various efforts to demonstrate the feasibility of reactor monitoring based on the detection of the Coherent Neutrino Nucleus Scattering (CNNS) process with High Purity Germanium (HPGe) technology. CNNS detection for reactor antineutrino energies requires lowering the electronic noise in low-capacitance kg-scale HPGe detectors below 100 eV as well as stringent reduction in other particle backgrounds. Existing state-of-the-art detectors are limited to an electronic noise of 95 eV-FWHM. In this work, we employed an ultra-low capacitance point-contact detector with a commercial integrated circuit preamplifier-on-a-chip in an ultra-low vibration mechanically cooled cryostat to achieve an electronic noise of 39 eV-FWHM at 43 K. We also present the results of a background measurement campaign at the Spallation Neutron Source to select the area with sufficient low background to allow a successful first-time measurement of the CNNS process.

ACKNOWLEDGMENTS

This work is supported by the Office of Defense Nuclear Nonproliferation Research and Development.

CONTENTS

FIGURES

TABLES

NOMENCLATURE

ASIC	Application Specific Integrated Circuit
BEGe	Broad Energy Germanium
CMOS	Complementary Metal Oxide Semiconductor
CNNS	Coherent Neutrino-Nucleus Scattering
CRY	Cosmic-ray Shower Library
DOE	Department of Energy
ENC	Equivalent Noise Charge
ENDF	Evaluated Nuclear Data File
FWHM	Full Width Half maximum
HDPE	High Density Polyethylene
HPGe	High Purity Germanium
JEFF	Joint Evaluated Fission and Fusion File
JFET	Junction Field Effect Transistor
IAEA	International Atomic Energy Agency
LBNL	Lawrence Berkeley National Laboratory
LMFE	Low-mass Front-End
LN	Liquid Nitrogen
LNC	Low Noise (Low) Capacitance (ASIC)
MJoule	mega joule = 10^6 Joules
MOS	Metal Oxide Semiconductor
m.w.e.	meters of water equivalent
NSC	Neutron Scatter Camera
ORNL	Oak Ridge National Laboratories
PPC	P-Type Point Contact
RMS	Root Mean Square
SNL	Sandia National Laboratories
SNS	Spallation Neutron source
SONGS	San Onofre Nuclear Generating Station
ULGeN	Ultra-Low Noise Germanium Neutrino Detection system

1. INTRODUCTION

This project aimed at the development, construction, and deployment of a large-mass High Purity Germanium (HPGe) detection system with the required ultra-low electronic noise threshold to demonstrate detection of reactor antineutrinos via the Coherent Neutrino Nucleus Scattering (CNNS) process. The coherent elastic scattering of a reactor antineutrino in a Ge detector target mass produces a recoiling Ge nucleus with an ionization energy smaller than 300 eV. Detecting such small signal requires an unprecedentedly low electronic-noise threshold not available in commercial detectors with the desired 1kg-scale target mass. As such, reducing the electronic noise threshold of kg-scale HPGe detectors to less than 100 eV is an essential and enabling objective in the pursuit of reactor monitoring with Ge technology.

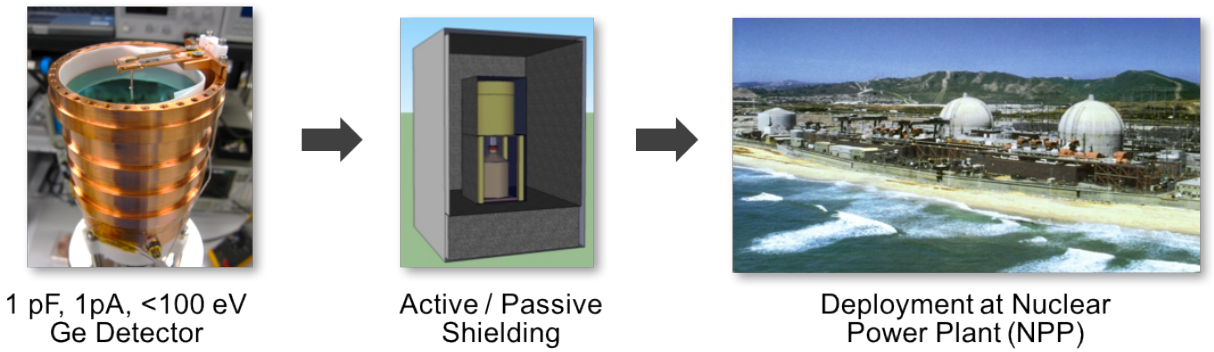

Figure 1: Diagram representing the evolution of the project starting goals.

Over the past decade, detection of antineutrinos to monitor nuclear power plants or to detect and monitor other nuclear activities related to the nuclear fission process, in close or standoff distances, has been an active research field, important for safeguards and non-proliferation. Other antineutrino detection systems rely on the inverse-beta decay process, which is characterized by a much smaller cross section than achievable through the CNNS process if sufficiently low energy threshold can be attained. Instead of large-scale and stationary detection systems, systems than rely on CNNS detection can be compact and potentially mobile, which could be easily incorporated into the global nuclear safeguards non-proliferation detection regime. Power-levels and fuel composition could be potentially measured more effectively with the CNNS process.

Advances in large-mass ultra-low noise HPGe technologies are also of great interest to the science community. In particular, experiments that will benefit from increase in detection sensitivity are those searching for weakly interacting particles or in general rare physics events related to weak interaction processes, such as the detection and characterization of the coherent neutrino nucleus scattering or the search for cold dark matter.

At the start of this project, the focus of our work was broken down into three high-level goals: the development and fabrication of kg-scale ultra-low noise Ge prototype detection system, the prototype deployment at the San Onofre Nuclear Generating Station (SONGS) reactor site for first time observation of CNNS, and the development and characterization of new ultra-low noise CMOS based readout. As result, the technical tasks naturally separated into electronic noise reduction work and particle background reduction and rejection work. During the first year, the electronic work focused on developing a JFET-based readout. Progress was made in reducing the electronic noise, but it became evident that a transformational improvement in noise would be necessary and only achievable with the exploration of alternate readout technologies. The background studies comprised simulations of the neutron interaction with the germanium and the different shielding materials, with the purpose to guide shielding design for a deployment at the belowground SONGS tendon gallery.

Two important developments during the first year of the project required an adjustment of the goals for the overall project and changes in the tasks associated with these:

1.) The JFET-based readout work revealed noise levels not yet sufficient for the detection of CNNS at a power reactor. During that time CANBERRA INC claimed to achieve as low as 80 eV FWHM (~240eV of threshold) with 1.5 kg of HPGe, indicating that the path to improve noise with JFET readout might be near exhausted. Further reduction of electronic noise is vital to the successful detection of power reactor antineutrinos, and we considered that a low-temperature CMOS readout had the potential to deliver the desired low noise performance.

2.) The permanent shutdown of the SONGS power station forced us to considered other feasible reactors and neutrino sources.

As a neutrino source, the Spallation Neutron Source (SNS) at ORNL offered a unique opportunity to enable the detection of the CNNS process. Since 2013, we have been actively involved in the forming of the multi-institutional COHERENT collaboration to measure CNNS at the SNS. While the SNS provides a significantly lower neutrino flux as compared to an operating nuclear power reactor, the higher neutrino energy and the beam timing should compensate for the neutrino deficiency and enable CNNS detection. The about ten times higher neutrino energy allows to use more conventional and existing HPGe detectors technologies (p-type point contact detectors with trigger thresholds of ~1 keV). The opportunity of deploying at the SNS should provide first-time confirmation of the existence of CNNS, which is of extraordinary relevance to the continued pursuit of its application in reactor monitoring.

Based on the above, the project goals were modified to: the development of CMOS-based low-threshold germanium detection technology, and background characterization for the first-time detection of CNNS at SNS. The electronic noise tasks then focused on the development of a prototype mechanically cooled CMOS readout system. In coordination with the NNSA Nuclear Science and Security Consortium (NSSC), a low temperature (8 K) cryostat was acquired and commissioned to investigate the physics of point contact Ge detectors and advanced JFET and CMOS readout electronics. The background tasks, on the other hand, focused on the measurement and characterization of the neutron and gamma backgrounds at the various SNS locations available for a Ge system deployment.

2. Electronic Noise Reduction

The abundant fluence of reactor antineutrinos suggests a novel approach must be sought for the monitoring of domestic and international nuclear reactors via their antineutrino flux. While existing antineutrino detection scenarios rely on inverse beta decay detected in extremely large volumes of liquid, we have proposed to follow a different neutrino interaction predicted by the standard model: coherent elastic neutrino nuclear scattering [1]. The significant cross-section of this interaction provides for a much more compact system, albeit with intrinsic size limits due to shielding constraints. The method relies on the liberation of small amounts of energy (hundreds of eV) following an antineutrino interaction with a germanium nucleus. Detection therefore requires a very low energy threshold detector of reasonable size. The germanium detector readout work performed at LBNL and described in this section closely follows and extends efforts within the MAJORANA neutrinoless double beta decay experiment [2] which rely on low background and low threshold ^{68}Ge p-type point contact (PPC) detectors [3]. Ultra-low noise thresholds are achieved with the LBNL-developed low-mass front end (LMFE) [4].

2.2. A Lower Noise JFET Solution

Low Mass Front End Electronics

The core of the LBNL LMFE is the junction field effect transistor, a device wherein a voltage at the *gate* modulates the resistance (and thus current) between the *source* and the *drain* terminals (i.e. a voltage controlled resistor). This device is the first component to see the induced voltage from the charge carrier movement within the crystal capacitance and serves to convert this voltage into an amplified current. The crystalline silicon that forms the source-drain channel shares many of the same requirements for crystal purity as the germanium crystal, and for this reason, noise in JFETs may vary in subtle or significant ways from lot to lot and from manufacturer to manufacturer. The input capacitance of the JFET must also match as closely as possible the small (~1 pF) capacitance of the germanium point contact (or small anode) detector. Following these requirements, we have selected MX11 JFETs from MOXTEK, Inc. (Orem, UT [5]) who have developed ultra-low noise JFET technologies, mainly for silicon x-ray detectors, which boast low input capacitance and low leakage current in a 1 mm^2 bare die package.

The remainder of the front end (Figure 2) includes the feedback resistor and feedback capacitor which form the amplifying portion of the charge-sensitive preamplifier loop which converts charge carrier movement in the crystal into a decaying step impulse. This continuous-feedback preamp requires a large (>10 GΩ) low-temperature feedback resistor for low-noise operation (unlike the more modern pulse-reset preamplifier). This leads to very long pulses (ms decay) which are deemed acceptable due to the extremely low event rate in antineutrino detection.

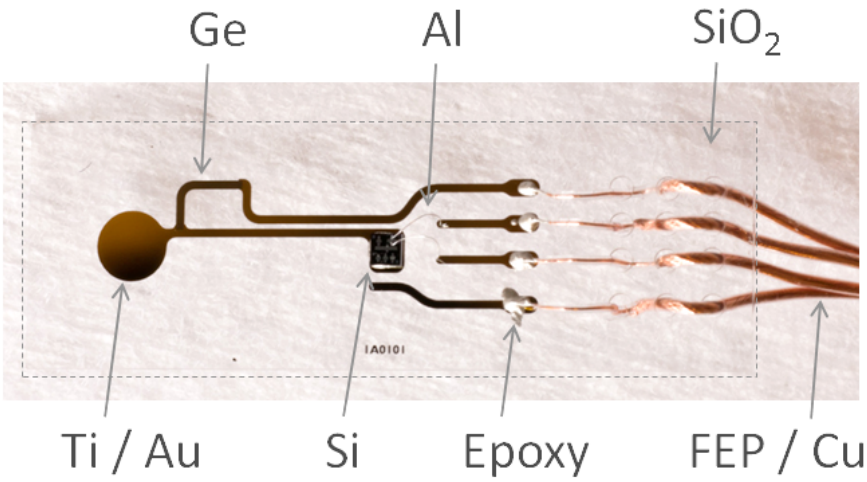

Figure 2: Materials of the Majorana LMFE (7 × 20 mm^2) with four picocoax cables threaded through ultrasonically drilled holes in the thin glass substrate. The feedback resistor is Ge, the JFET is Si, the bond wires are Al.

The JFET and feedback components are epoxied or patterned onto a fused silica glass substrate located in close proximity to the point contact face of the crystal in order to minimize additional parasitic capacitance. The feedback resistor is a sputtered amorphous germanium (a-Ge) film whose resistance increases dramatically at lower temperatures. Small bond wires connect the JFET to photolithography-patterned gold traces and cables are epoxied onto traces in order to communicate with the warm side of the preamplifier. Materials are chosen so as to emit a low fluence of low energy particles which might be detected in the region of interest. Through low-background counting facilities and mass spectrometry, materials are selected which contain low quantities of uranium and thorium.

Mechanical and Thermal Considerations

The LMFE is held by its non-cable side only in a copper clip (Figure 3) maintained near liquid nitrogen temperature (80-100 K). Because the JFET has a constant current of ~10 mA flowing through the source-drain channel, a significant amount of heat (~40 mW) must conduct through the silica substrate. The silica is made thin (0.2 mm) so as to limit thermal conduction and raise the JFET temperature to an ideal operating point (150-200 K). This establishes a thermal gradient from the gate pad to the JFET. The temperature-dependent value of the a-Ge resistor will then clearly depend on placement relative to this thermal gradient. Varying the current in the JFET may then affect the temperatures of both the JFET and the feedback resistor, which may have several incoherent effects on the equivalent noise charge.

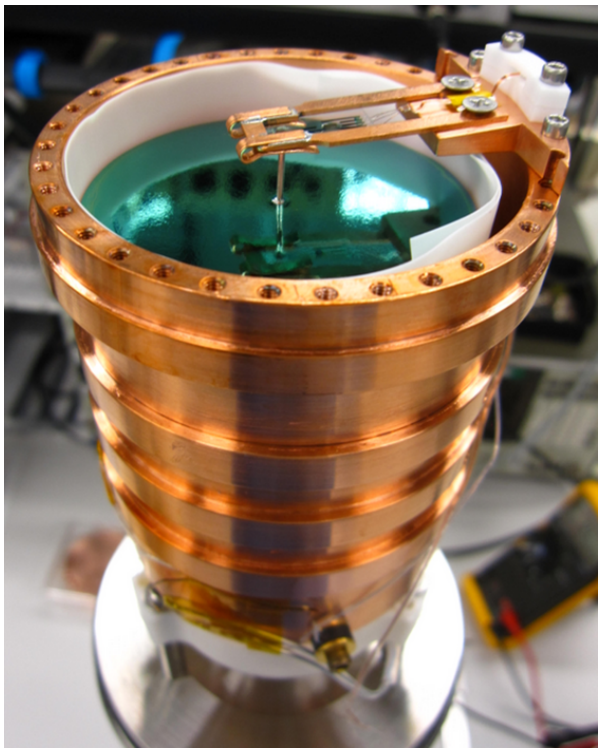

Figure 3: LMFE mounted above the point contact face of a 900 g PPC in a modified low background dipstick cryostat, suitable for deployment in an existing shield at a reactor.

Because the LMFE is cantilevered from one side and the copper clip is suspended over a large crystal, vibrations may induce microphonic noise which is particularly noticeable at longer shaping times. Mechanical damping of the LMFE and clip are employed to limit vibrations. Sized slightly larger than the gap between crystal point contact and LMFE gate pad, the copper gate pin also serves to mechanically damp the LMFE and clip. Care must be taken to not exert excessive force which would break the thin glass substrate. For testing of the LMFE without detector, we similarly damp the clip to prevent microphonic vibrations. It became necessary to later explore alternative wire bonding methods to remove this pin from the system and create a more reliable lower capacitance point contact connection.

Electrical Connections

Cables connected to the source, drain, feedback, and pulser lines of the LMFE run some 30 cm to the warm components of the charge sensitive preamplifier (Figure 4). Three additional transistors boost the signal before it is buffered and amplified by one final stage (not shown). The long-decay signal is then filtered or shaped by traditional nuclear pulse processing electronics so that a Gaussian or trapezoidal pulse shape is obtained. Once the system calibration is known (amplifier voltage vs. energy deposited), only the baseline root-mean-square (rms) voltage noise of the amplifier is measured. This rms voltage is directly related to the system resolution in eV-FWHM. With each shaping time, a different frequency window is selected and effects from various electron interactions within the system can be probed. At higher frequencies (shorter shaping times), the voltage noise from the JFET tends to dominate, while at

lower frequencies the current noise from detector leakage current, lower feedback resistances and microphonics dominate.

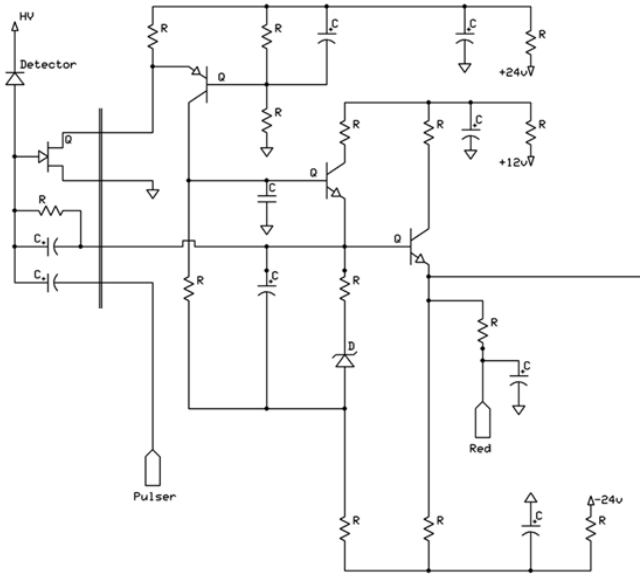

Figure 4: Schematic of the LBNL LMFE charge sensitive preamplifier. Cold components of the LMFE at the left connect directly to the point contact of the PPC crystal.

In order to ensure values of LMFE feedback and pulser capacitors are as designed, a 3D electrostatic simulation (Figure 5) is performed in the finite element analysis package COMSOL. Fine features are carefully meshed in 3D, and the Poisson equation is solved to yield the electric fields between traces. Surface integration of charge provides the capacitances between pairs of traces. When compared with careful bench measurements in a shielded probe station with a calibrated LCR meter, simulations coincide within the measurement error.

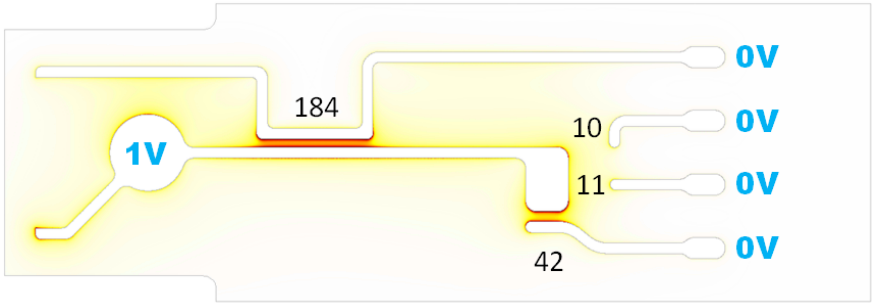

Figure 5: Two-dimensional slice of the 3D electric field strength from an electrostatic simulation in which 1 V is placed on the gate pad at the left. Inter-trace capacitance values in fF (10^{-15} F) are indicated between traces. The feedback capacitor is 184 fF, while the pulser capacitor is 42 fF.

Equivalent Noise Charge Components

The rms voltage from the shaping amplifier baseline (5-10 mV) at each shaping time is converted to electrons-rms-squared or mean-squared electrons. For reference, 100 eV-FWHM in Ge correlates to 14.3

electrons-rms (2.355 rms/FWHM, 2.95 eV/electron-hole pair). In order to accurately compare shaping times, the FWHM of the voltage vs. time signal is used. The voltage ("series"), current ("parallel") and 1/*f* noise components are fit to the equivalent noise charge curve (Figure 6) and compared between experiments to determine incremental improvements. This work began with the existing Majorana LMFE coupled to a 900 g LBNL PPC, located inside a modified Canberra low background cryostat, with a lowest electronic noise figure of 141 eV-FWHM.

Reducing the detector-related noise requires creating a lower capacitance and lower leakage PPC detector for which LBNL has demonstrated previous capability. Thus, efforts were first focused on reducing the noise components of the LMFE without the complications of convolving detector and LMFE noise responses. Further, the current noise component of the LMFE derives primarily from the feedback resistance and microphonics, so the voltage noise of the LMFE was addressed first.

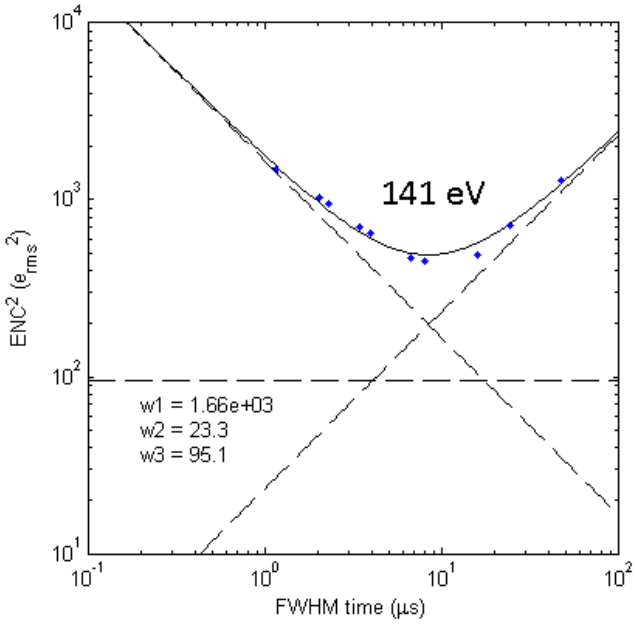

Figure 6: Equivalent noise charge squared (electrons) vs. FWHM of shaped pulse (μs) for Majorana LMFE with 900 g PPC detector at 101 K. Fitting coefficients w1-3 represent voltage ("series"), current ("parallel"), and 1/f noise components.

As the temperature of the cryostat increases from LN temperatures, the voltage noise of the JFET is reduced, to a point. However, the feedback resistance decreases with temperature, thus increasing current noise. The JFET temperature was optimized through several factors: cryostat temperature, thermal conductivity to cryostat and JFET power (voltage and current). The voltage noise component was reduced from 1660 (Figure 6) to 582 (Figure 7).

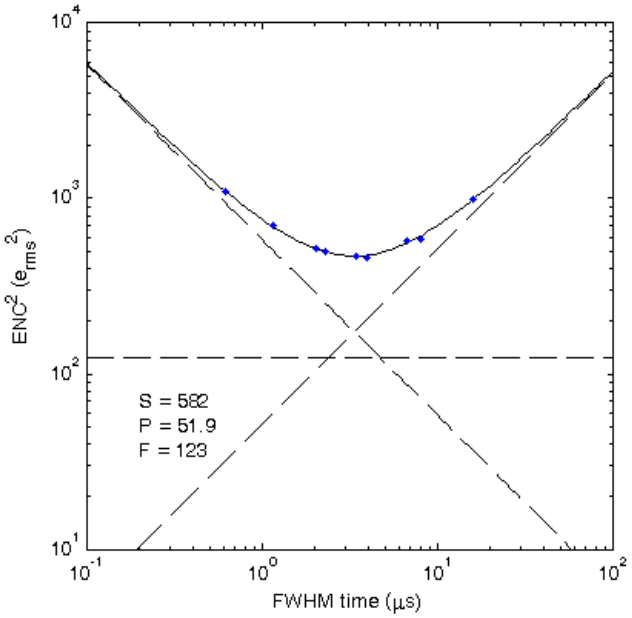

Figure 7: Equivalent noise curve for LMFE with tuned JFET current at a cryostat temperature of 110 K. The voltage noise component is 582, compared to 1660 from Figure 6.

However, the associated increase in parallel noise component required a new feedback resistor to be fabricated. Several revisions were made to increase the value with thinner depositions, less-wide patterning, increased length and locations away from the hot JFET. Progress has brought current LMFE noise levels without detector down to 95 eV-FWHM in a low temperature dipstick cryostat. Because the dipstick cryostat of a deployable detector (with sufficient accommodations for shielding) will mandate a temperature closer to 100 K, the LMFE must be refined to achieve a higher feedback resistance at elevated temperatures.

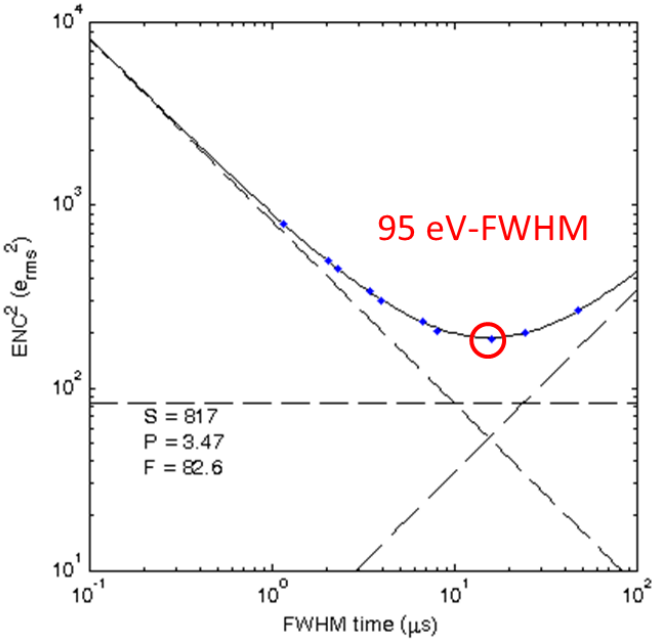

Figure 8: Equivalent noise curve for LMFE at 79 K, illustrating low parallel noise, but slightly higher voltage noise than the previous figure.

The crystal leakage current apparent at more elevated temperatures is also a concern for operation at longer shaping times.

It was around this time in the second year of the project that Canberra had announced it was capable of manufacturing kg-scale detectors with electronic noise resolutions as low as 95 eV-FWHM, apparently fueled by requests from Chinese customers surrounding dark energy experiments. Through discussions with Canberra engineers, it was confirmed that methods employed to reach this performance relied upon the additional heating of the JFET by a separate low-noise heating resistor circuit. This fact, combined with the unplanned shutdown of the San Onofre Nuclear Generating Station (SONGS) reactor, moved the focus of this project squarely onto the development of advanced CMOS-based readout of mechanically cooled HPGe detectors.

2.3. Improvements over Traditional JFET Readout

The electronic noise observed at the output of a charge sensitive preamplifier can be described in terms of the equivalent noise charge (ENC), a sum of voltage, 1/*f*, and current noise terms:

$$\mathrm{ENC}^2 = F_v \frac{4k_B T}{g_m} \frac{C_{\mathrm{in}}^2}{\tau_p} + F_{1/f} A_f C_{\mathrm{in}}^2 + F_i \left(2q_e I_{\mathrm{in}}\right) \tau_p \qquad (1)$$

where Fv, $F_{1/f}$; and F_i are: voltage, 1/*f* , and current noise factors defined by the choice of shaping function. The voltage noise of the FET is proportional to its temperature T and inversely proportional to its transconductance, g_m. The capacitance $C_{\mathrm{in}} = C_{\mathrm{det}} + C_{\mathrm{FET}} + C_{\mathrm{fb}} + C_{\mathrm{test}} + C_{\mathrm{stray}}$ includes all capacitances at the field effect transistor (FET) input: detector, FET gate, feedback, test, and stray. Methods for reducing C_{in} include: altering electrode geometries to reduce the detector capacitance (C_{det}), selecting a lower input

capacitance FET (C_{FET}), and reducing the feedback capacitor (C_{fb}). A capacitor for test pulses (C_{test}) at the input should be a very small fraction of C_{in}. The design of crystal and FET support structures should be carefully planned to minimize the stray capacitance (C_{stray}) to all nearby conductors. The voltage noise term is inversely proportional to the peaking time τ_p.

The $1/f$ noise factor A_f is dependent on dielectric properties and fabrication processes, however its impact on the ENC is significantly reduced in ultra-low C_{in} systems. The current noise I_{in} includes leakage currents from both detector and FET and is scaled by the electron charge q_e. While not explicitly stated, the leakage current can typically be improved by lowering the temperatures of detector and FET. The current noise term is directly proportional to τ_p. Microphonic noise, not included in Eqn. 1, is generally observed at larger peaking time τ_p. Several issues with existing HPGe detectors may complicate the further reduction of electronic noise. Typical cold front end electronics require some form of thermal standoff complicating their placement very near the detector, thus increasing C_{in}. Liquid cryogens increase operational complexity and induce microphonic noise from boiling. Extremely low C_{det} (<1 pF) HPGe crystals may be difficult to contact with conventional spring-loaded pins. Lower temperatures achievable with mechanical cooling improve leakage current and mobility in silicon transistors and germanium detector crystals, but typical cryocoolers introduce excessive microphonic noise.

Having fully investigated the limits of the LBNL JFET-based LMFE technology, three specific areas for further improvement were identified, namely: lowering the temperature of detector and front end, moving from JFET to MOSFET front end transistor, and lowering the capacitance of detector and front end. Improvements made in each of these areas are detailed in the sections below, and detailed in a recent NIM-A publication [5].

2.3.1. Vibration-Free Mechanical Cooling

While liquid nitrogen (LN_2) is sufficient for cooling HPGe detectors, the lower temperatures (down to 4 K) achievable by mechanically refrigerated cryocoolers are beneficial to improving leakage currents and carrier mobilities, as the lower phonon population reduces the likelihood of lattice scattering. Semiconductor surfaces and electrical contacts made to semiconductors generally have lower leakage currents at lower temperatures, thereby reducing noise. At low enough temperatures, charge carrier concentrations at the FET contacts may be reduced to a level where they are said to “freeze out”, degrading or preventing operation. At extremely low temperatures, charge trapping in the HPGe bulk may be a concern.

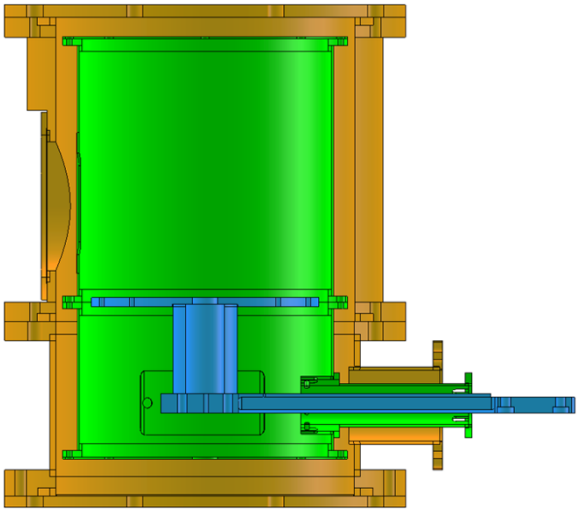

Figure 9: Cross-section view of the ARS cryostat, with 8 K cold finger and detector stage (blue), 40 K first stage infrared shield (green), and outer 300 K vacuum shell (gold).

Sub-LN_2 temperatures were achieved in this project with a Gifford-McMahon (GM) cryocooler (model DE-204) from Advanced Research Systems. A 3.5 kW water-cooled compressor was connected through flexible compressed helium lines to a cold head expander affixed to a cantilevered floor stand, while a vacuum cryostat (Figure 9) was mounted to a steel table which was isolated from the floor. Vibrations from the significant displacement of the cold head (up to 100 µm at 10 m/s^2) were eliminated with a scheme employed in low temperature optical microscopy (see Figure 10) wherein the cryostat cold finger is disconnected from the cold head and heat is instead communicated through atmospheric pressure helium gas.

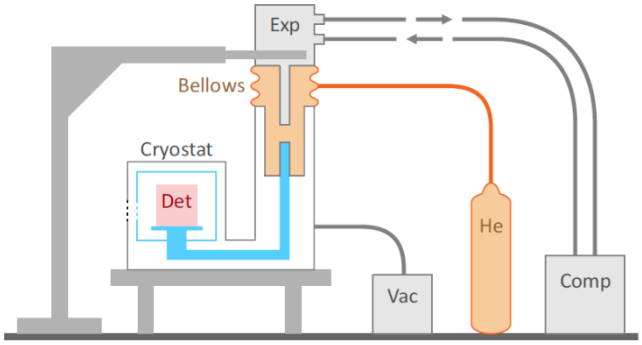

Figure 10: The ultra-low vibration GM cryocooler consists of a compressor and expander (i.e. cold head) which cool a separate volume of atmospheric pressure helium, which then cools the cold finger of a vacuum cryostat, housing a point contact HPGe detector and front end electronics. The cryostat and expander are mechanically connected only through a rubber bellows.

A flexible rubber bellows contains the helium and a 0.5 psi pressure is maintained during temperature transitions through venting or addition of 99.999% pure helium (although balloon grade appears to work just as well). This configuration achieved its base temperature of 8 K in 5 hr, and a Kapton foil heater on the cryostat cold finger enabled operation up to room temperature.

The cryocooler system from ARS was delivered with LBNL-specified customizations to their ultra-low vibration optical cryostat (model DMX-20), which was fabricated from nickel-plated aluminum and oxygen-free high-conductivity (OFHC) copper. The cryostat was then further modified to house our detector and readout electronics. The inner 100 mm diameter by 100 mm thick chamber was enclosed by an infrared shield held at the primary stage temperature of ~40 K. Small gaps in the shield were included for pumping, but were minimized to reduce the admission of thermal radiation which would increase the observed detector leakage current. The infrared shield contained an aluminized mylar window, aligned with a 0.33 mm thick beryllium window in the outer vacuum shroud. The cryostat was actively pumped to 10^{-6} Torr to reduce the possibility of contaminant adsorption onto the HPGe point contact surface. Any vibrations from the flexible stainless steel vacuum hose appeared not to have impacted the measured noise performance, as verified by briefly powering down the pump during active measurements.

2.3.2. MOSFET Front End Electronics

Electronic noise in the charge sensitive preamplifier is typically dominated by contributions from the first field effect transistor (FET) in the front end electronics, for which two specific devices are commonly employed. The junction FET (JFET) has been the traditional choice due to its low 1/ f noise and low voltage noise when cooled. Similar in operation is the metal oxide semiconductor FET (MOSFET) as found in complementary MOSFET (CMOS) processes, which provide for integration of the entire charge sensitive preamplifier as well as additional signal processing.

The optimization of noise in the typical silicon JFET requires elevation of the temperature (above ~120 K) with some thermal standoff or heater, which can increase stray capacitance at the JFET gate. Custom JFETs which function down to 4 K are not available with the low (< 1 pF) capacitance required for ultra-low noise detector front end electronics. While the transconductances of both JFET and MOSFET improve continually as the temperature is lowered, the relatively high minimum operating temperature of JFETs directly support the use of MOSFETs below LN_2 temperatures where HPGe leakage currents may also improve.

Although MOSFETs tend to have higher $1/f$ noise factors than their JFET counterparts, an ultra-low capacitance system will reduce the impact of the $1/f$ noise term in the ENC (see Eqn. 1). Low MOSFET capacitance can be obtained through proper design, while low JFET capacitance is typically limited to the selection from available devices.

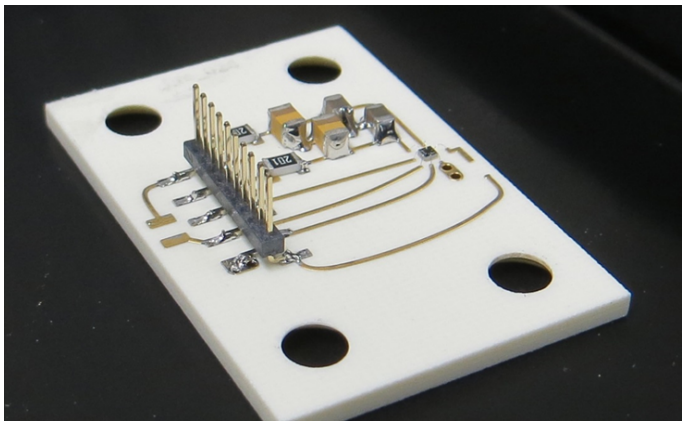

Figure 11: The “CUBE” ASIC (right), bonded to a low-loss PCB, with power supply filtering surface mount resistors and capacitors for its two power supplies.

While CMOS front ends have been integrated with higher capacitance HPGe detectors, much lower capacitance CMOS front end electronics have been developed for low capacitance (~0.1 pF) silicon drift detectors (SDD). The “CUBE” application specific integrated circuit (ASIC), developed by XGLab is such a CMOS charge sensitive pulse-reset preamplifier-on-a-chip, exhibiting remarkably low electronic noise. Encouraged by applications of the CUBE to other HPGe detectors, we integrated this ASIC with a LBNL ultra-low capacitance PPC detector. The 0.75 × 0.75 mm^2 CUBE die (prototype version PRE-024) was epoxied to a floating pad on a 60 mil Rogers-4350 low dielectric loss printed circuit board (PCB) with electroless nickel immersion gold (ENIG) traces (see Figure 11). Caution was exercised in preventing MOSFET damage from electrostatic discharge. Pads on the ASIC were ultrasonically wedge bonded to PCB traces with 1 mil Al(1% Si) wire. The board also contained two identical RC bypass filters (see Fig. 3) for the V_{SSS} = −3.0 V and V_{IO} = +3.3 V ASIC power supplies, composed of size 0805 components: 200 Ω metal film, 47 µF tantalum, and 47 nF ceramic C0G. A separate test pulse trace was provided on the PCB, whose parasitic capacitance to the input pad was simulated and measured to be 0.010 pF.

Signal and power wires from the CUBE PCB were routed through several infrared and vacuum feedthroughs to an external XGLab-supplied “Bias Board” (ver. 7), which filtered the ±10 VDC from a standard bench power supply, supplied reset logic and level control, and buffered the CUBE output with a gain of −2.25.

2.3.3. Low Capacitance Detector

The large volume point contact HPGe detector was originally developed to lower the electronic noise in large mass n-type detectors for the direct detection of weakly interacting particles. The small electrode of this configuration yields a detector capacitance on the order of 1 pF, compared to the tens of picofarads for traditional coaxial germanium detectors. The similar p-type point contact (PPC) detector has found utility in several neutrino and astroparticle physics experiments.

The PPC HPGe detector used in this work was employed previously to demonstrate the low-noise capabilities of the low-mass front end (LMFE) electronics developed for the Majorana Demonstrator.

This 20 mm diameter by 10 mm thick detector originally had a 1.5 mm diameter point contact with a concave dimple for alignment of a tensioned pin contact. The detector previously had a capacitance of 0.47 pF and had exhibited sub-pA leakage current through many temperature and vacuum cycles over several years. The outer n-type hole-blocking contact was formed by lithium diffusion, while the bipolar blocking point contact was formed by sputtered amorphous silicon (a-Si).

The detector described above was modified to obtain a lower capacitance through the combination of an even smaller point contact electrode and the use of wire bonding for the interconnection between the detector and the front end electronics.

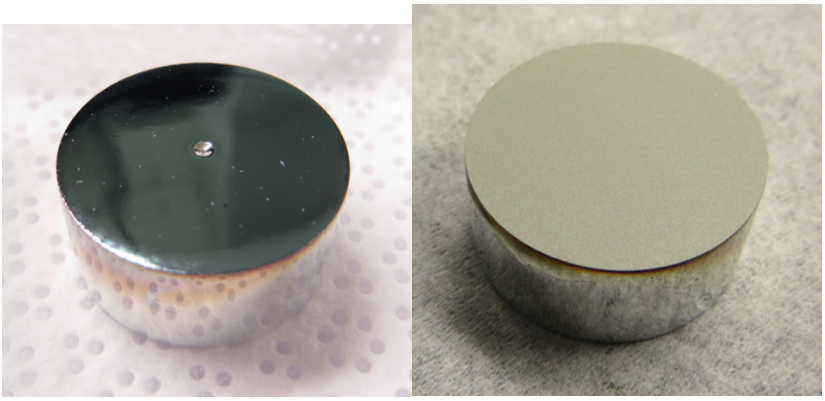

Figure 12: Original PPC detector with concave dimple (left) and removed (right).

To modify the detector, the point contact face was hand-lapped (600 grit SiC) to remove the dimple (Figure 12) which was incompatible with wire bonding. A 4:1 HF:HNO_3 etch was performed to remove any lapping damage. A new layer of a-Si was sputtered onto the point contact face, and an 8 kÅ aluminum film was evaporated through a 0.75 mm diameter hole shadow mask (Figure 13) to form the point contact electrode.

Figure 13: Chemically etched stainless steel shadow mask for defining the evaporated aluminum point contact.

The crystal was mounted in a spring-loaded, indium-lined aluminum clamp, held at a positive high voltage bias. This assembly was mounted onto a boron nitride (Saint Gobain AX05) high voltage insulator. A silicon diode temperature sensor was affixed to a prototype crystal to ensure the detector temperature adequately tracked that of the cold finger.

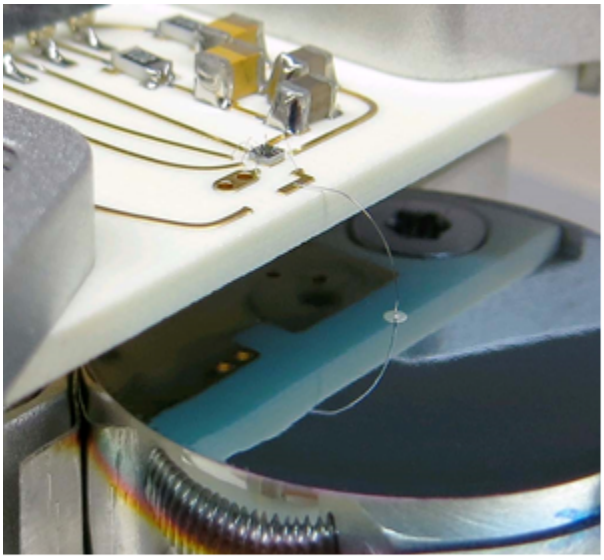

Figure 14: CUBE ASIC and PPC detector with wire bonded point contact in mechanically cooled cryostat.

The 0.75 mm point contact of the detector was ultrasonically wedge bonded with 2 mil aluminum wire to a trace on the PCB shared by the wire bond to the preamplifier input (as in Figure 14).

2.3.4. Ultra-Low Noise Germanium Detector Integration

Once the detector and ASIC were mounted in the cryostat, care was exercised in maintaining signal integrity of the high voltage bias and preamplifier output signals. The signal chain is illustrated in Figure 15.

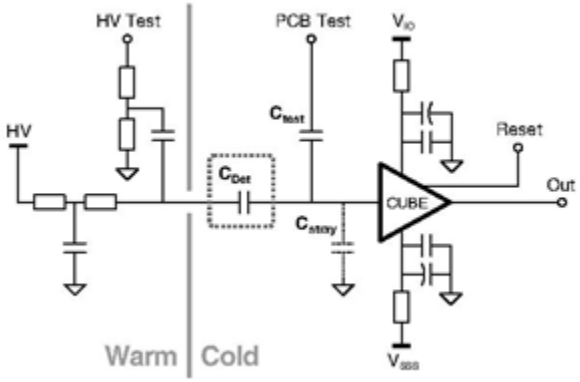

Figure 15: Front end signal chain, including CUBE power supply filters. Test pulse capacitors are included both before (HV Test) and after (PCB Test) the detector.

Detector bias was supplied by a Canberra 3002D high voltage power supply. A high voltage RC low-pass filter (100 MΩ, 10 nF), in a box (Figure 16) just outside the cryostat, removed significant voltage fluctuations, and an associated resistive divider provided for injection of charge through a step voltage pulse onto the detector capacitance.

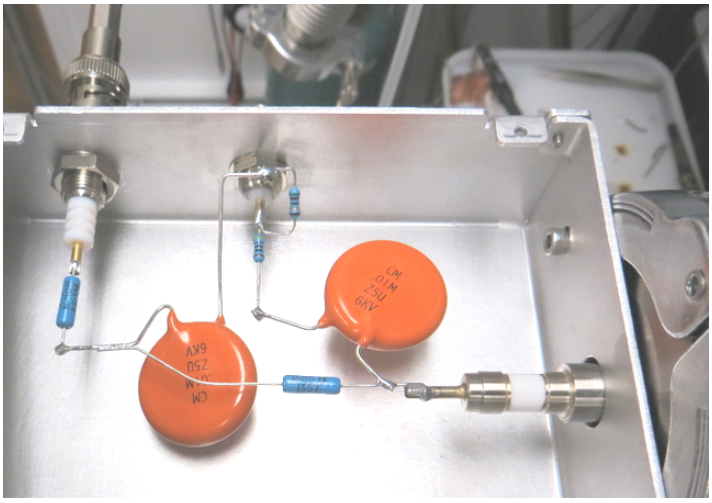

Figure 16: High voltage RC filter and HV pulse injection box.

After mechanically, electrically and thermally securing and verifying all connections (Figure 17), the cryostat was closed up and pumped to a vacuum of ~10^{-6} Torr prior to cooling.

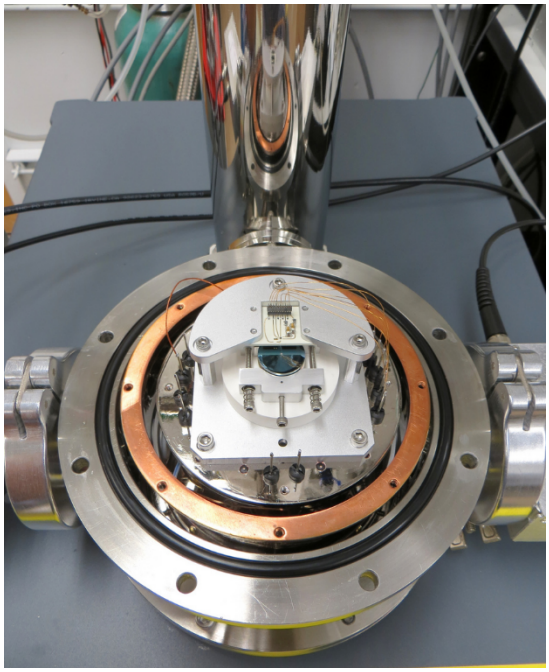

Figure 17: PPC detector and CUBE ASIC in ARS 4K Cryostat, with 4K, 40K and 300K shields removed.

The two parameters of a HPGe detector with the greatest influence on electronic noise are its depleted capacitance and its leakage current. In this section, we first present the detector capacitance and leakage current measurements made with our ultra-low noise detector system. Measurements are then given for the energy resolution and equivalent noise charge as a function of temperature and peaking time.

2.3.4.1. Detector Capacitance

The capacitance of the detector was measured by applying a known voltage step ΔV_{pulse} onto the high voltage electrode of the detector. The resulting charge pulse measured by the preamplifier, as calibrated with the 59.5 keV peak from an Am-241 source, is then equal to the product of ΔV_{pulse} and the depleted capacitance C_{det}. As the high voltage bias is increased, the depleted region grows, and the capacitance decreases until the detector is fully depleted.

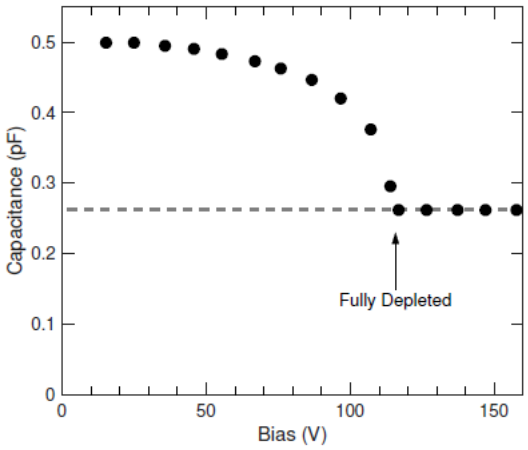

Figure 18: PPC detector capacitance as measured by pulse injection through a high voltage filter capacitor. The full depletion voltage is 120 V, beyond which the detector capacitance is 0.26 pF.

The full depletion voltage of the crystal was determined to be 120 V from measurements of the capacitance as a function of applied bias (Figure 18). The 0.26 pF capacitance at full depletion of this detector (a 45% reduction from the previous detector design) agreed well with 3D electrostatic simulations performed with the finite element modeling package COMSOL [43].

2.3.4.2. Leakage Current

The leakage current $I_{leak} = Q_{FS}/t_{reset}$ was determined from QFS, the calibrated full scale charge and t_{reset}, the time between preamplifier reset pulses. The leakage current as a function of applied bias was measured at multiple temperatures as the cryostat was cooled. At 500 V above full depletion, the current remained less than twice that at full depletion, indicating stable performance of the detector when overdepleted. The leakage currents measured at 150 V were observed (Figure 19) to drop by approximately an order of magnitude with every 10 K of cooling from 150 K to 100 K. Below 100 K, the leakage current was < 0.1 pA, with a minimum of 0.020 pA at 30 K. Additional tests will be needed to determine the specific origin of the currents measured at low temperatures.

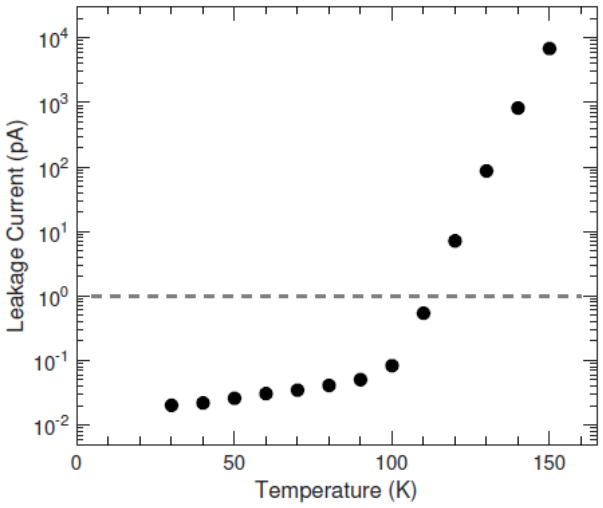

Figure 19: Leakage current as measured by pulse reset intervals, when the detector was biased at 150 V. The dashed line at 1 pA is for visual reference.

2.3.4.3. Energy Resolution

The flux from an uncollimated ^{241}Am source was directed through the beryllium window toward both the lithium contact and point contact faces of the detector. The buffered preamplifier output was filtered by a pair of Canberra 2026x semi-gaussian shaping amplifiers with peaking times that ranged from 0.2 µs to 53 µs. Pulse heights were measured by an Amptek MCA8000D multi-channel analyzer (MCA). The resulting energy spectrum at 43 K is shown in Figure 20 for a 400 V bias and 18 µs peaking time. The electronic pulser peak width of 39 eV-FWHM is among the lowest measured with a HPGe detector of this size.

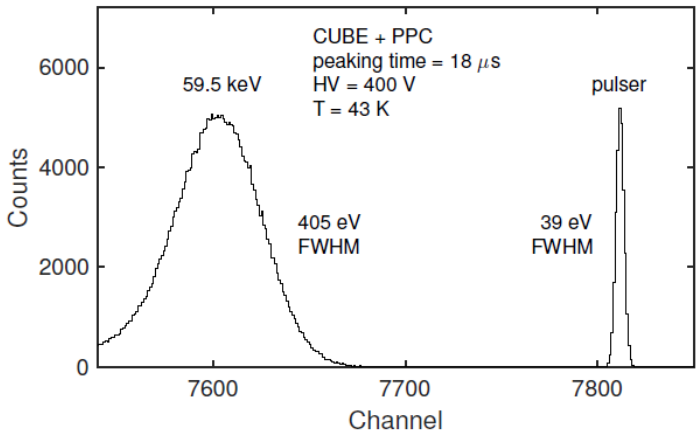

Figure 20: Spectrum of ^{241}Am indicating the 59.5 keV gamma line from the source and a pulser peak with a width of 39 eV-FWHM.

Calibrated baseline rms voltages from the shaping amplifier were sampled at 50 MSa/s on an Agilent DSOX-3054A 500 MHz bandwidth oscilloscope to calculate the ENC in electrons-rms. The standard

deviation (i.e. rms voltage) of several million samples between radiation events compared closely to rms voltages from an analog 20 MHz bandwidth rms meter (Boonton 93A). The 39 eV-FWHM value was independently verified with the 5.6 electrons-rms determined by the calibrated 2.6 mV-rms baseline voltage of the shaping amplifier.

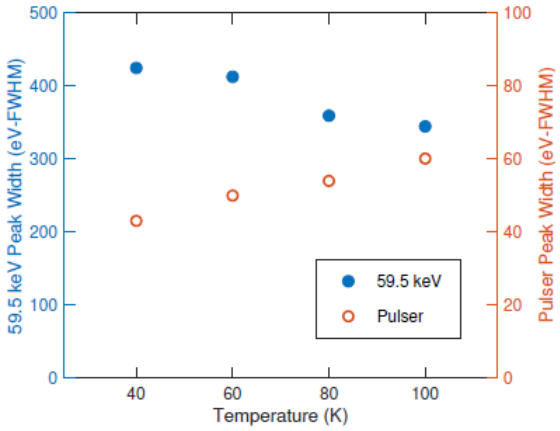

Figure 21: Spectrum peak widths for ^{241}Am 59.5 keV (left axis) and pulser (right axis), at an applied bias of 150 V, and peaking time of 53 µs.

Gaussian fits to the 59.5 keV peak appeared to be broader than that expected when assuming a reasonable Fano factor. Preliminary measurements indicated an improvement in resolution as the temperature was raised above 40 K (see Figure 21), while a slight degradation was observed in the electronic noise. The minimum resolution observed at 59.5 keV was 345 eV-FWHM, which represents a derived Fano factor of 0.122, neglecting incomplete charge collection. No signal processing was performed to remove slow signals from degraded surface events. Results will be reported separately on the impact of temperature and bias on the charge collection and contact properties of this particular detector and the associated noise of the preamplifier ASIC. The full characterization of the low energy spectral performance of this crystal was left for future work with more suitable low energy contacts.

2.3.4.4. Electronic Noise

The ENC curve (vs. peaking time) of the low capacitance PPC with CMOS preamplifier in the low vibration cryostat at 43 K (Figure 22) indicates the minimum pulser peak width of 39 eV-FWHM. The previous lowest noise performance of this crystal with a low mass JFET front end was 85 eV-FWHM. The primary factor responsible for this improvement was the decreased capacitance of detector and FET, each about 40% to 50% of their previous values. This lower capacitance improved both voltage noise and the relative contribution of 1/*f* noise.

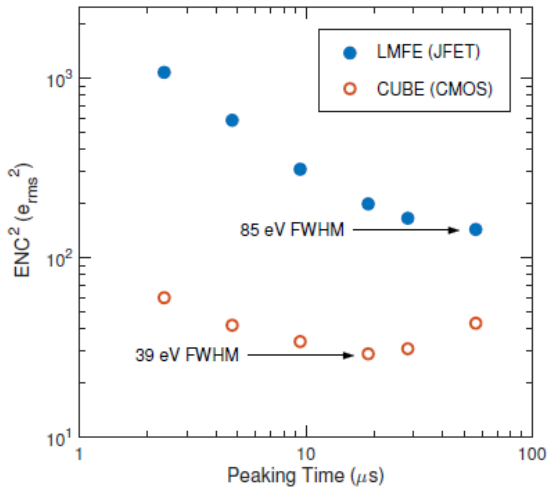

Figure 22: Equivalent noise charge (from spectral peak widths) versus peaking time of PPC with CUBE CMOS ASIC at 43 K and 400 V bias. The minimum resolution of 39 eV-FWHM from pulser peak widths is equivalent to a noise of 5.6 electrons-rms. The previous low noise limit of 85 eV-FWHM is shown for this crystal in its higher capacitance configuration with LN_2 cooling and a cold JFET [24].

The lower temperature improved leakage currents in both FET and detector, and reduced thermally related voltage noise at shorter peaking times. Continuous reduction of voltage and current noise was observed (Fig. 9) as the temperature was lowered from 110 K to 50 K (and below).

2.3.5. Summary of Improvements over JFET

Three specific barriers to lowering electronic noise in detection systems were identified and overcome in this work to create a uniquely low noise HPGe detector technology.

First, excessive vibrations from conventional mechanical cooling (30 to 80 K) would significantly degrade the performance of low noise germanium detectors. Boiling liquid cryogens also cause microphonics which limit low noise performance at longer peaking times. Our detector system operated down to 30 K and eliminated microphonics by employing a technique from cryogenic microscopy which employs an atmospheric pressure heat exchange gas with a conventional GM cryocooler.

Second, the detector capacitance of commercially available HPGe detectors is typically limited by point contact sizes and stray capacitances (e.g. from spring-loaded pin contacts). We reduced the detector capacitance to 0.26 pF by wire bonding to a 0.75 mm diameter detector electrode.

Third, the noise of the JFET in conventional detectors must be optimized by raising its current and temperature, increasing the complexity of operation. We integrated an ultra-low capacitance PPC detector with a commercially available ultra-low noise CMOS preamplifier-on-a-chip ASIC, whose performance improves down to 30 K.

Implications for Antineutrino Detection

Three key elements of a successful coherent elastic neutrino-nucleus scattering measurement are: low radioactive backgrounds, a large detector mass, and a low energy threshold. To illustrate the impact of

electronic noise and energy threshold on the antineutrino detection rate, we consider a typical energy distribution of electron antineutrinos from a 1 GW nuclear power reactor. The expected number of antineutrinos detected through Ge nucleus recoils in a given time with a given detector mass is illustrated (Figure 23) for three electronic noise levels.

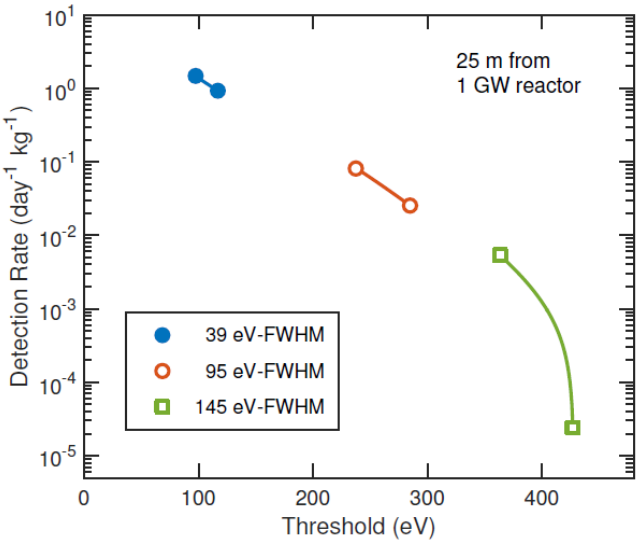

Figure 23: Simulated number of reactor antineutrinos detected, per day, per kg of Ge, at 25 m from a 1 GW reactor. The minimum threshold ranges (2.5 to 3.0 times FWHM noise) are shown for three electronic noise levels.

The noise level of 95 eV-FWHM represents the lowest noise performance of the low mass front end demonstrated during development of the Majorana Demonstrator. In this work, a detector technology was presented with a 39 eV-FWHM noise level which would increase the anticipated antineutrino detection rate by several orders of magnitude from the previous deployment at 145 eV-FWHM, while maintaining capabilities for larger mass detectors in a suitably low background configuration.

2.4. Future Improvements in Low Noise Electronics

While the very impressive low capacitance low noise CUBE preamplifier on a chip performed exceptionally well when paired with a low capacitance PPC HPGe detector, several aspects of this ASIC could be refined to provide a truly ground breaking level of performance.

First, the number of readout lines and requisite cables all have an impact on the readout complexity, but more importantly on the intrinsic radioactive background the detector sees from materials in close proximity. It would therefore be advantageous to reduce the required number of power supplies and readout lines.

Second, we anticipate being able to fabricate detectors with extremely small capacitances, and therefore the capacitance of the front-end MOSFET in the preamplifier ASIC should also be small as well. Additional ASIC layout tricks may need to be employed to sufficiently reduce all capacitances seen by the first input transistor.

Third, every ASIC requires power supply bypassing / filtering capacitors to be located as close as possible to the ASIC. These tend to be higher value capacitors, not typically fabricated in silicon or with thin film processes. Typical methods for power supply bypass capacitor fabrication involves ceramic-like materials which tend to be extremely radioactive (relative to our low background baseline). It would therefore be advantageous to incorporate some form of active filtering on the ASIC itself to reduce the need for local power supply capacitors. This may also, in the future, enable the application of direct bonding the preamplifier to the HPGe detector itself.

2.4.1. A New Low Noise Low Capacitance (LNC) ASIC

Collaborating with Brookhaven National Laboratory, we worked together to design a new charge sensitive preamplifier ASIC for extremely low detector capacitances. The first requirement of reducing the number of connections was to move from a dual power supply system to a single supply system. At the same time the reset signal was removed by applying a resistorless continuous feedback system. Because high value (Gohm) resistors are not available in CMOS technology, the high impedance of transistors is instead used to provide low-noise continuous feedback path without requiring an external feedback resistor. This has the effect of improving the number of antineutrinos observed at low energies by removing radioactive background from nearby components.

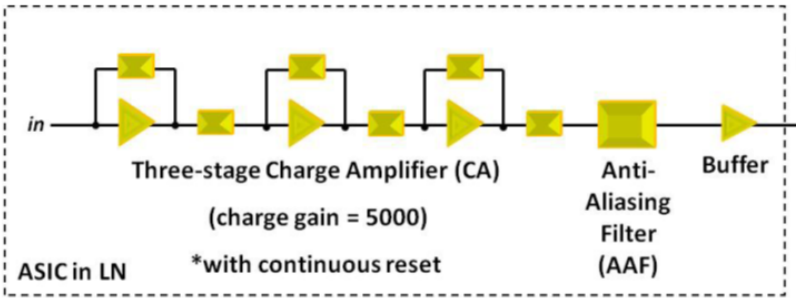

Figure 24: Architecture of the cold front-end ASIC prior to warm ADC and digital shaper.

The resistorless continuous feedback scheme is detailed in Figure 25 below.

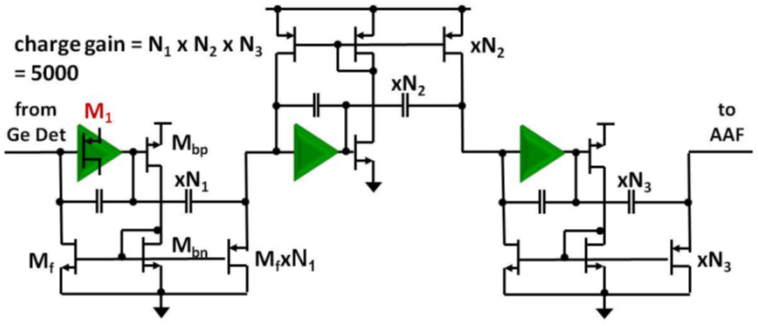

Figure 25: Simplified schematic of the three-stage charge amplifier with continuous reset configuration.

The final connection scheme for this LNC preamp-on-a-chip comprises 4 traces: power, ground, input, output. No simpler scheme exists. This is particularly advantageous for multi-detector systems which can share power and ground, thus reducing the requisite number of vacuum feedthroughs.

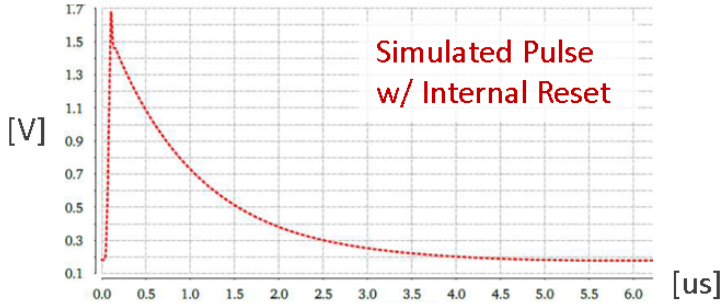

Figure 26: Simulated input current and output voltage signals of the front-end ASIC given a 50-ns input pulse.

The preamplifier output signal maintains a 50 MHz bandwidth (Figure 26) while being able to drive signals over 1 m away to the input stage of a fast ADC and waveform digitizer.

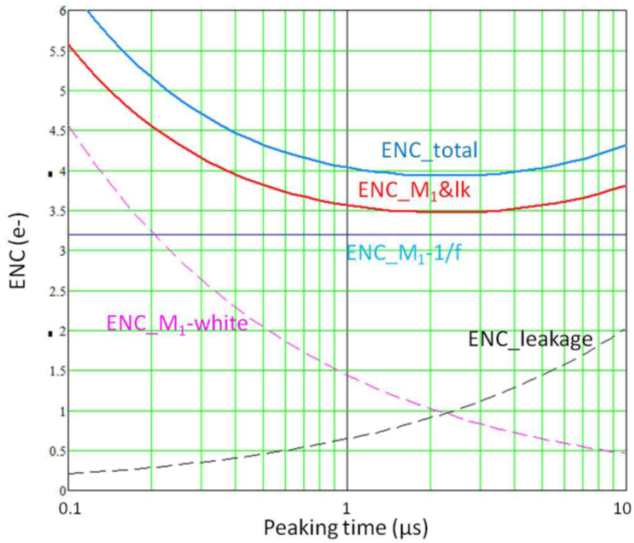

Figure 27: Simulated ENC contributions versus peaking time, assuming a detector capacitance of 0.100 pF.

The anticipated equivalent noise charge at 40 K was carefully simulated (Figure 27) to be 4 electrons-rms (28 eV-FWHM) with a 0.100 pF detector. This easily allows for detector thresholds below 100 eV-threshold.

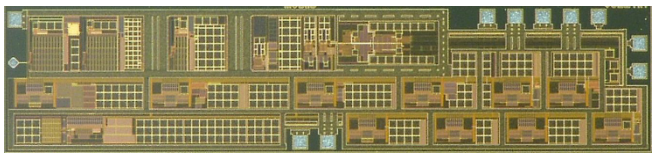

Figure 28: Photograph of fabricated LNC ASIC die, designed by BNL, fabricated in 0.18-µm CMOS technology.

Due to the inevitable delays in ASIC design and fabrication, the final ASICs fabricated and delivered (Figure 28) were not able to be sufficiently tested prior to the end of this project. Test results of this ASIC will be presented at the 2017 IEEE NSS. Additional tests are planned through application in neutrinoless double beta decay experiments, where a deep underground ton-scale HPGe PPC array is planned, and for which this ASIC shares the same requirements as that of reactor antineutrino monitoring. We look forward to further advancing and scaling this technology to prove its viability for reactor deployment in the near future.

Electronic Noise References

1. B. Cabrera-Palmer, D. Reyna, J. Steele, et al., "Coherent Neutrino Nuclear Scattering With Germanium," *presented at Applied Antineutrino Physics Workshop, Vienna*, 2011.

2. V.E. Guiseppe et al., "The MAJORANA Neutrinoless Double-Beta Decay Experiment, " 2008 *IEEE Nucl. Sci. Symp*., Conference Record, N22-1, 2008.

3. P.N. Luke, F.S. Goulding, N.W. Madden and R.H. Pehl, "Low Capacitance Large Volume Shaped-Field Germanium Detector, " *IEEE Trans. Nucl. Sci*. vol. 36, no. 1, 1989.

4. P. Barton, P. Luke, M. Amman, et al., “Low-Noise Low-Mass Front End Electronics for Low-Background Physics Experiments Using Germanium Detectors,” *IEEE Nucl. Sci. Symp.*, N40-6 (2013).

5. P.Barton, M.Amman, R.Martin, K.Vetter, " Ultra-low noise mechanically cooled germanium detector,” *NIM-A* 812, p17-23, 2016.

3. RADIATION BACKGROUND STUDIES FOR A REACTOR DEPLOYMENT

Once down to 100-eV electronic noise threshold, the radiation background counts in the Ge active material would have to be controlled to extremely low levels. Our calculations showed that the observation of the SONGS reactor On/Off transition with 3σ confidence level require a 30-day measurement time at an integrated background rate of less than 10 counts per [kg·day] in the region 0.1 keV - 1 keV.

The dominant background source in that energy region are neutrons that can produce Ge-nucleus recoils identical to the antineutrino signal. The background neutrons mainly originate as secondary particles in cosmic-ray showers or are produced by muons interacting in surrounding materials, with energy extending to hundreds of MeV. Neutrons also activate the Ge nuclei, which decay emitting X-rays and Auger electrons internal to the germanium. Cosmic protons can similarly activate the Ge nuclei, though they are present at lower rates. Working with a 500-eV threshold Ge detector, the CoGeNT collaboration [1] discovered that partial energy depositions from these X-rays interacting near the Ge surface dead layer produce a significant near-threshold continuum of events. Finally, natural gamma-ray radioactivity form detector materials can also contribute to the low-energy background continuum.

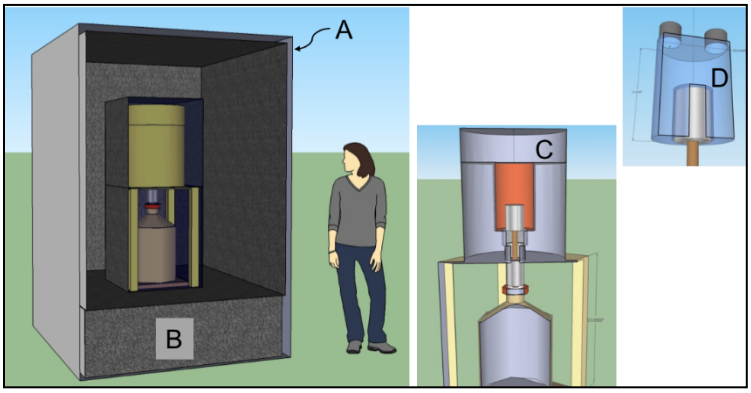

Figure 29: Full shielding planned for a reactor deployment at SONGS tendon gallery. (A) muon veto panels, (B) HDPE neutron moderator with internal borated polyethylene, (C) lead shield, and (D) a plastic scintillator inner veto.

Our proposed shielding design for a reactor deployment, sketched in Figure 29, was composed of: (A) 2-inch external high-efficiency muon veto panels, (B) a 20-inch High Density Polyethylene (HDPE) neutron moderator with internal borated Polyethylene as thermal neutron absorber, (C) a Canberra Ultra Low Background Lead shield, and (D) a plastic scintillator inner veto for fast neutrons and gamma-rays. This shielding was conceived to fit in SONGS tendon gallery, which would have provided a 30 m.w.e overburden against cosmic radiation. Building the detector components near the Ge crystal out of radio-clean materials was considered as important as robust shielding. Note that beta and alpha particles from materials close to the Ge crystal are suppressed by the ~1-mm Lithium-diffused n+ contact covering most of the crystal surface in p-type point-contact Ge detectors. As shown in [1], the X-ray partial energy depositions in this dead layer can be rejected by their slower rise time. Additional planned measures for

background reductions were to purge radon gas out of the lead shield with nitrogen gas, and to wait once deployed at the tendon gallery for the decay of cosmogenic activated nuclei.
Our background studies first focused on characterizing the neutron interaction events within the Ge crystal based on the GEANT4 [2] Monte Carlo simulation package. We then moved on to building a GEANT4 model of the full system and studied the shielding effectivity on different energy neutrons.

3.1. Verification of GEANT4 low energy neutron physics

Given the stringent limits on the allowed background counts (< 10 counts per [kg·day]) in the CNNS very low energy range (0.1 keV - 1 keV), we started our simulation work by verifying the results from the GEANT4 neutron interactions models. We employed a toy model consisting of a mono-energetic neutron beam perpendicularly incident on the flat face center of a 60 mm × 60 mm cylindrical Ge crystal, and ran it in the GEANT4 versions 9.5.p01 and 9.6.p01 for incident neutron energies ranging from 10^{-4} MeV to 200 MeV. We compared the results from various GEANT4 physics lists that use the data driven high precision (HP) neutron package to transport neutrons below 20 MeV down to thermal energies. For incident neutron energies $E_n \leq 20$ MeV, the cross-sections—and thus, the interaction rates—derived from our GEANT4 simulation for the neutron elastic, inelastic and capture interactions with each of the naturally-occurring Ge isotopes agree with the experimental nuclear reaction database ENDF cross-sections [3] within 5 to 10 %. Figure 30 shows the comparison of the experimental and simulated cross-sections for the ^{70}Ge, which constitutes about 20 % of natural germanium. For incident neutron energies $E_n > 20$ MeV, we observed divergences up to 25 % between the cross-sections derived from the GEANT4 simulation and the experimental values reported by the JEFF Nuclear Data Library [4].

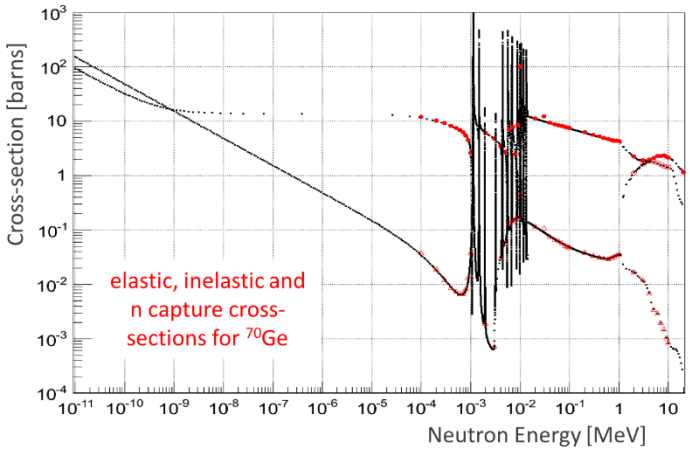

Figure 30: Comparison of the (n,^{70}Ge) cross-sections calculated from our GEANT4 toy simulation and the experimental values reported by ENDF [3]. The calculated elastic cross-section is shown as red filled circles, the inelastic cross-section is shown as red open circles, and the neutron capture cross-section is shown as red open triangles. All the experimental values are shown as black dots.

We also used the toy model to verify energy conservation in the GEANT4 interactions given the importance of correctly accounting for small energy depositions when estimating the background for a CNNS measurement. For that, we calculated the energy difference ΔEnergy equal to the sum of the incoming particles energies minus the sum of the outgoing particles energies for each interaction. We found that a large portion (~ 20%) of neutron elastic scatters with incident energy > ~10 MeV deposit excess energy which could take values above 100 eV. For inelastic interactions, we also found events with energy deficit as well as energy excess in the final particles (see example of Figure 31), probably due to the incorrect emission of gamma-rays originated by the Ge nucleus de-excitations. Although the energy discrepancies were found to be in general small in energy and frequency, this study showed that it is important to keep track of such events when estimating rates above the very small 100-eV threshold.

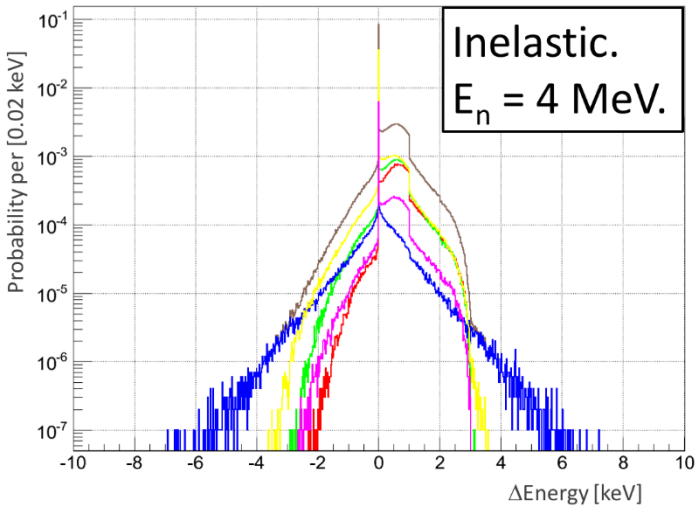

Figure 31: Probability, per incident 4-MeV neutron, of GEANT4 inelastic interactions violating energy conservation by ΔEnergy. Each color represents a different natural Ge isotope, except brown which represents the sum for all isotopes.

We also calculated the probability of events with total deposited energy in the spectral region 0.1 to 3 keV, which is defined as the integral number of counts in that region divided by the total number of simulated incident neutrons. The results, presented in Table 1 for each simulated energy, show that neutrons with energies around 10 keV to 100 keV have the highest probability of depositing energy in our region of interest via Ge nucleus recoils generated from neutron elastic interactions.

Incident neutron E_n =	**1 keV**	**10 keV**	**100 keV**	**1 MeV**	**10 MeV**	**100 MeV**
depositions from **all** processes	0.0007	0.396	0.732	0.121	0.081	0.057
recoils from neutron elastic scatters	0	0.040	0.741	0.149	0.126	0.077
recoils from neutron inelastic scatters	0	0	0.005	0.038	0.002	0.0004
recoils from neutron capture	0.0014	0.007	0.007	0.0005	0.002	0.0004

Table 1: Probability per incident neutron of producing an event with energy in the spectral region 0.1 to 3 keV. The first row corresponds to the total event energy irrespective of the interactions processes. The remaining rows consider only nuclei recoil depositions generated from the neutron elastic, inelastic and capture interactions, respectively.

In point-contact Ge detectors, the signal rise time depends on the interaction site within the crystal. This allows identification of events consisting of coincident interactions in different crystal sites that produce signals with different rise times; though the ability to discriminate multi-site interactions strongly depends on the energy deposited in the individual interactions and the noise threshold. As anti-neutrinos only produce single-site interactions, filtering multi-site interactions is an important component of background rejection [5]. In particular, neutrons with energies around 10 keV to few hundred keV have a significant probability of scattering more than once within a large Ge crystal volume compared to higher energy neutrons. Figure 32 shows the histograms of the number of nuclei recoils for incident neutron energies E_n = 100 keV and 100 MeV. The 2D histograms of Figure 33 plot the incident neutron final scatter position before leaving the crystal or being captured, and also show that higher energy neutrons are more likely to punch through without interacting or interacting only once, while ~100-keV neutrons tend to scatter around the crystal.

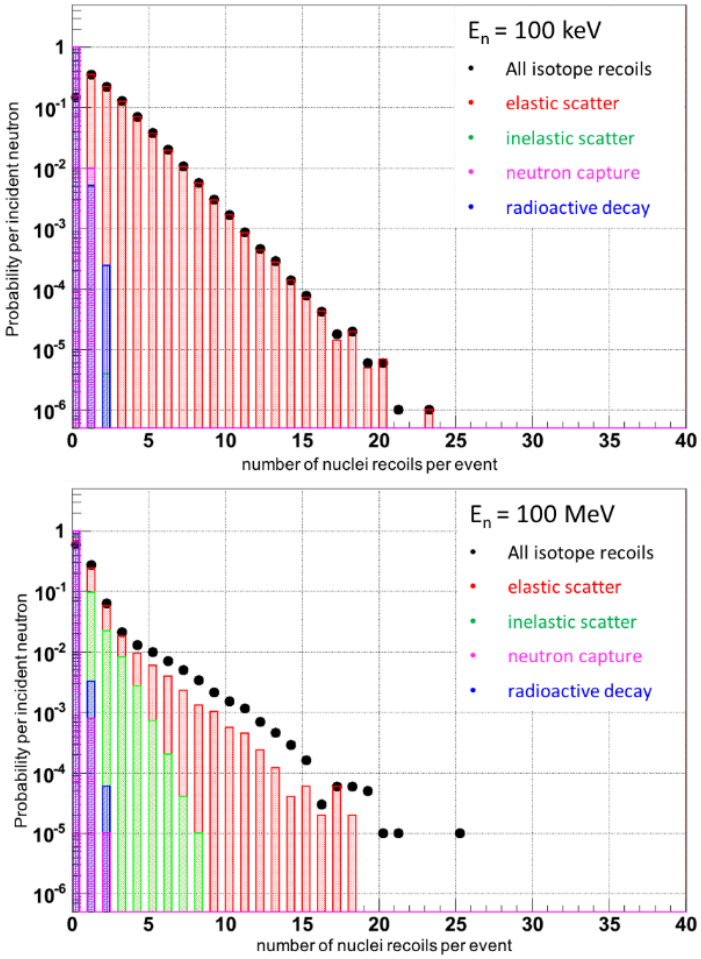

Figure 32: Number of nuclei recoils within the simulated Ge crystal volume per incident neutron. Top: incident neutron energy equal to 100 keV. Bottom: incident neutron energy equal to 100 MeV.

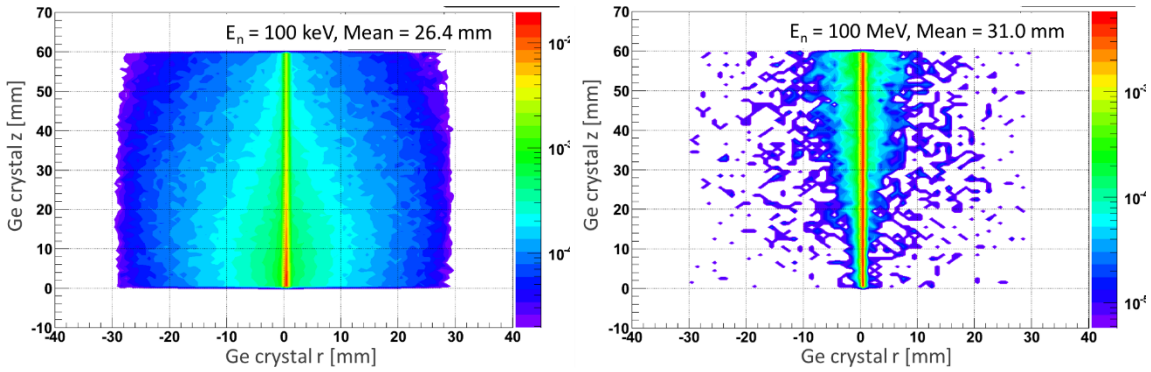

Figure 33: Position of the final scatter of the incident neutron before leaving the crystal or being captured. Left: incident neutron energy equal to 100 keV. Right: incident neutron energy equal to 100 MeV.

3.2. Shielding simulations

In order to guide the design and fabrication of the detector and the shield assembly, we constructed the GEANT4 model of the full system (detector and shielding). To simulate the cosmic background, we built in our model the SONGS tendon gallery with 30 m.w.e overburden, and implemented two different cosmic particle generators: a cosmic muon generator based on experimental data [6] and the Cosmic-ray Shower Library (CRY) [7]. However, these comprehensive cosmic background simulations had not been completed and analyzed by the time the news of SONGS permanent shutdown compelled us to change our Life Cycle Plan. Instead, we completed preliminary simulations that allowed to understand and evaluate the effect the various shielding components on the neutron background.

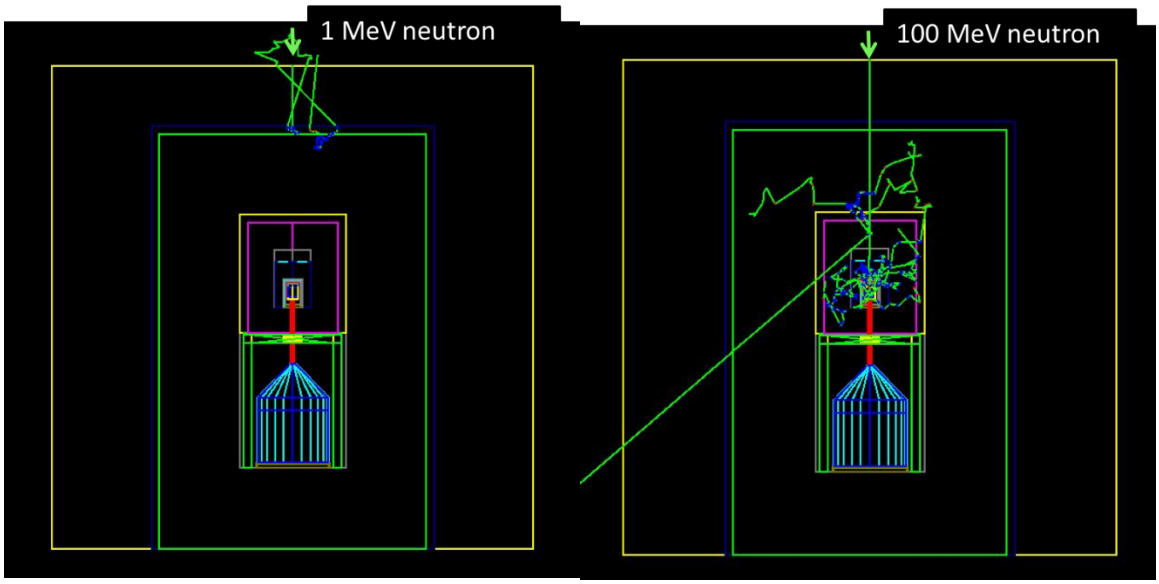

Figure 34: Visualization of the GEANT4 full shield model showing that few-MeV neutrons are easily moderated and deflected by the shielding while higher energy neutrons tend to penetrate and create multiple particles in the shielding.

As illustrated in Figure 34, neutrons of less than a few MeV are highly moderated and deflected by the thick HDPE layer. On the other hand, neutrons of higher energies have a higher probability of penetrating the HDPE layer and producing multiple particles that can reach and interact in the Ge detector. Figure 35 shows the Ge detector spectra in the region 0.1 keV to 1 keV from a simulation of a 50 MeV neutron beam vertically incident on the center of the top muon veto panel. The black-line spectrum represents all the events depositing energy in the Ge detector. The red-filled spectrum has been filtered to only contain single-site events, reducing the background rate by 40 %. The green spectra of Figure 36 has been obtained after further rejecting Ge events in coincidence with muon veto events— mainly due to gamma-rays from the high-energy neutron shower—, but shows no significant effect since the muon veto's role is to reject muon-related events. However, further rejection of Ge events in coincidence within a 0.1μs time window with inner veto events (with the inner veto threshold set to 100 keV) significantly reduces the background rate by another ~60%. This results lends support to having a plastic scintillator inner veto to shield fast neutrons and gamma-rays, which represents a departure from other experiments [1] that instead employed inorganic scintillator (like NaI(Tl)) inner veto and were sensitive to gamma-rays but not fast neutrons.

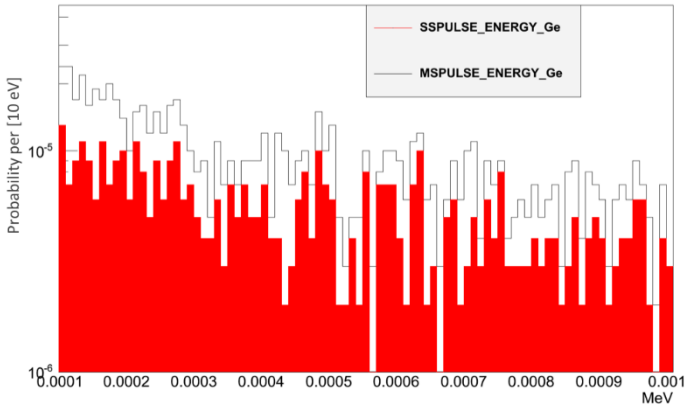

Figure 35: Ge detector spectra from a simulated 50 MeV neutron beam vertically incident on the center of the top muon veto panel. Black line spectrum: all events. Red filled spectrum: only single-site events. The spectra have been normalized by the number of incident neutrons.

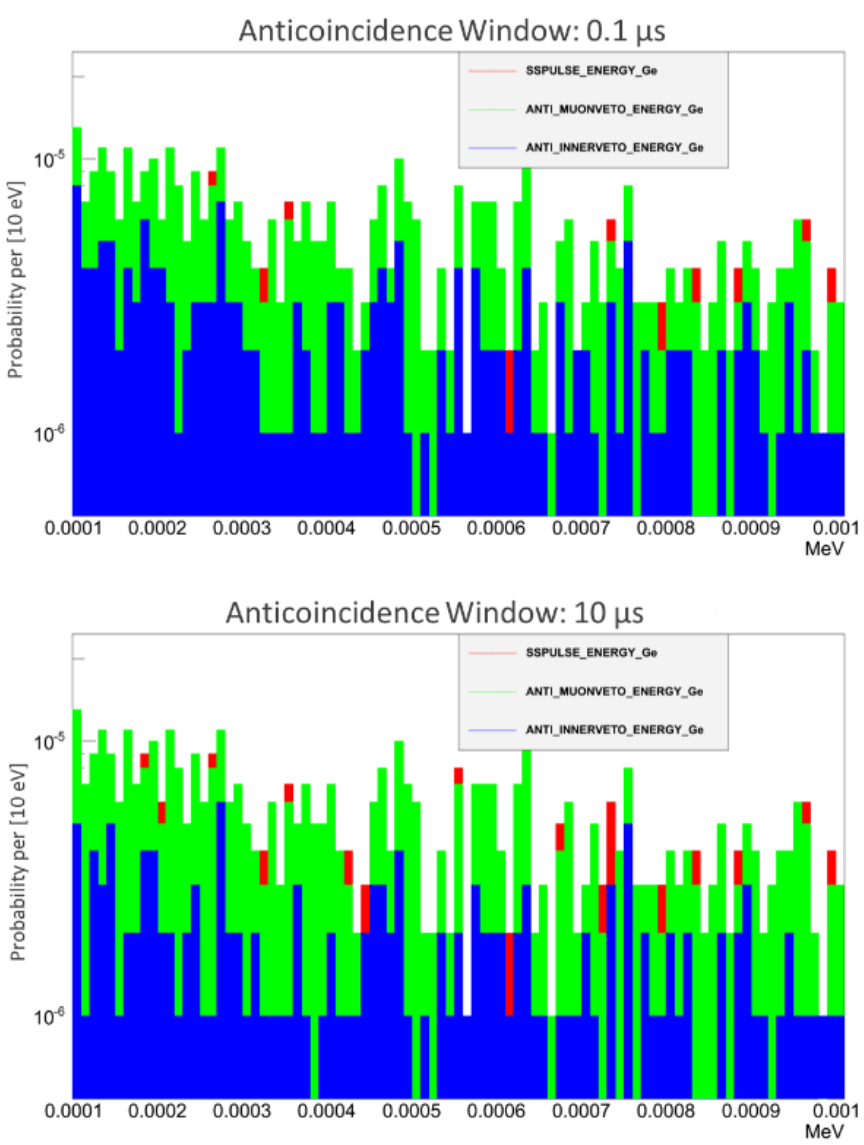

Figure 36: Ge detector spectra from a simulated 50 MeV neutron beam vertically incident on the center of the top muon veto panel. Red filled spectra: only single-site events as in Figure 35. Green filled spectra: after further filtering out muon-veto coincident events. Blue filled spectra: after further filtering out inner-veto coincident events within a 0.1 μs (left plot) and 10 μs (right plot) time window. The spectra have been normalized by the number of incident neutrons.

4. NEUTRON BACKGROUND CHARACTERIZATION FOR THE FISRT MEASUREMENT OF CNNS AT SNS

As a neutrino source, the Spallation Neutron Source offers a unique opportunity to enable the first-time detection of the CNNS process. The SNS neutrinos, with energies up to ~ 50 MeV, produce Ge recoils up to ~25 keV of detectable ionization energy. The detection of these more energetic recoils is possible with *existing* PPC HPGe detectors with threshold ~ 1keV. Due to a lower neutrino flux of ~10^7/cm^2/s at SNS (compared to ~10^{12}/cm^2/s at a nuclear power plant reactor), a Ge target mass of about tens of kg will be required, but that is easily attainable with current HPG technology [8].

The SNS beam is pulsed with 60 Hz frequency and <800 ns width arrival time of protons on target. This allows the reduction of steady-state radiation backgrounds—mainly gammas, neutrons and muons—by a factor close to 10^4. On the other hand, an intense high energy neutron flux originates from the SNS target at beam-on time and represents the main background for the CNNS detection.

Since FY14, the background task focused on the characterization of neutron backgrounds at several SNS locations suitable for a CNNS experiment deployment. For that purpose, the SNL-developed Neutron Scatter Camera (NSC) was upgraded to be sensitive to the neutron energy range up to few hundreds of MeV. In section 4.1, we describe the NSC hardware and data analysis modifications that enabled this extension in detectable incoming neutron energy.

During the course of three years, the NSC collected extensive data in five different locations: two experimental hall locations and three basement locations. The scheduling of each data collection period depended on the SNS beam-on schedule and on the SNS personnel and local ORNL colleagues available to move the NSC to the various locations. Data was also collected in each location during beam-off periods to measure the steady-state background baseline due to cosmic and natural radiation neutrons. As shown in section 4.2, the analysis of these data presented challenges depending on location due to variability in the radiation flux. At the end of this campaign, the last measured basement location (labeled basement C4) was selected as the main candidate for the deployment of a Ge system. This location should have the largest signal-to-noise ratio among all measured locations due to its very low measured background and an expected stronger neutrino signal given its proximity to the SNS target.

A secondary goal of this work was to generate an estimation of the background neutron flux that could serve as input to shielding simulations. However, as it will be discussed in section 4.1, the unfolding of the intermediate energy neutron flux from the NSC measured rates is a challenging task that did not fit in the scope of this project. Though we have attempted to estimate the NSC efficiency at these higher energies by comparing to the cosmic neutron spectral flux reported by others [9], our analysis of section 4.1.2 invalidates such simple energy bin comparison due to the large smearing of the NSC measured spectra, especially at the neutron energies above ~10 MeV.

4.1. Modifications to the Neutron Scatter Camera for intermediate neutron energies

The NSC is a fast neutron spectrometer and imager developed and progressively improved at SNL for more than a decade [10]. Its operational principle is based on the kinematic reconstruction of an event consisting of two neutron elastic scatters, where the energy and angular direction of incoming neutrons are calculated. This requires the measurement of the energy E_0 deposited in the first scatter, and the time of flight and distance to the second scatter to determine the scattered neutron kinetic energy $E_{n'}$. Then, the simple formula $E_n = E_0 + E_{n'}$ reconstructs the incoming neutron kinetic energy, while the neutron scattering angle given by $\theta = \text{acos}^{-1}\left(\sqrt{E_{n'}/E_n}\right)$ back-projects a conical surface containing the incoming neutron direction. With sufficient scattering events, a source image and spectrum can be produced [1].

Initially built to search for special nuclear materials, the NSC was configured to be most highly sensitive to the neutron energy range from 1 to 10 MeV. In its current version, the instrument consists of 2 arrays of 16 cells filled with EJ-309 [11] mounted in two parallel planes, with each cell individually read out by fast photomultiplier tubes (Hamamatsu H6527). All cells are 13 cm in diameter, with the length of those in the front plane chosen to be 5 cm in order to reduce the probability of multiple scatter, and the length of the back-plane cells chosen to be 13 cm to increase the probability of the second scatter. The distance between planes is adjustable, and a separation of 49.5 cm has been used for the data presented in this paper. Further details on general NSC design choices and their motivation can found in [10].

Organic scintillator is the detection medium, therefore instrument can still detect higher energy neutrons, albeit with less efficiency. Applications that benefit from such operating modality are experiments where neutrons of intermediate energies ~10-200 MeV are present, possibly together with lower energy neutrons, and represent a background to the detection of other particles. Examples are neutrino experiments at particle accelerators [8], where spatial, temporal and spectral characterization of neutron fluxes can provide useful information for experimental design, from shielding to timing. In the following subsections, we describe the adaptations done to the existing NSC to extend its functionality to intermediate-energy neutrons, and discuss the ultimate limits on the instrument's operational range.

4.1.1. Operation at Intermediate Energies

4.1.1.1. Instrument Modifications

In order to expand the NSC detectable range up to intermediate neutron energies of 200 MeV, time-of-flight (*TOF*) values as low as ~1 ns have to be resolved. For that, the data acquisition has been upgraded to consist of two 16-channel SIS3316 250MS 14-bit VME digitizers [12] able to yield about 1.5 ns in timing resolution. Furthermore, proton recoils due to intermediate-energy neutrons can reach tens of MeV-electron-equivalent (MeVee) compared to the < 3 MeVee recoils from fast neutrons, and thus, proportional readout response has to be extended to such energy depositions. In order to accept large scintillator pulses, the digitizers input range is set to the maximum available value of 5 V. Muon events,

which deposit 30 to 40 MeVee in average when traversing the middle of the scintillator cells, are used to adjust the gains of each cell's photomultiplier tube (PMT) so that the full muon pulses fall within the digitizers input range. Since each channel is independently calibrated, exact matching among all of the different PMT gains is not required.

4.1.1.2. Event Processing

Timing Resolution

The maximum sampling frequency sets the digitizer's timestamp precision to 4 ns. If this were the limit to the instrument time resolution, it would severely restrict our efficiency to measuring energies above ~10 MeV, but it is not. In order to improve beyond the event timestamp resolution, we record the pulse waveform and determine the pulse peak time by interpolating between points before and after the zero crossing of the waveform's first derivative. Since the rise time of scintillator pulses are constant and independent of the pulse height, the time of the pulse peak relative to the first waveform sample is simply added to the digitizer's timestamp.

Figure 37 shows an example histogram of the time between two consecutive gamma-ray interactions occurring in cell 7 (in the front plane) and cell 18 (in the back plane). As it will be explained in the next section, the plotted times have already been adjusted by existing hardware time offsets. That most of the histogram events correspond to gamma rays that Compton scatter in one cell and then interact again in the other cell is evidenced by the resultant distribution, which approximates a double Gaussian distribution with peak separation about twice the gamma-ray time-of-flight $t_{TOF}^{\gamma} = d/c$ between the cell pair. The double Gaussian fit of the histogram produces a standard deviation $\sigma_t \cong 1.5\ ns$, which is typical for all cell pairs. This σ_t also contains the spread time-of-flights due to the variation in gamma-ray scatter positions within the finite-size cells, so that it can be decomposed into

$$\sigma_t^2 = \sigma_d^2 + \sigma_{TOF}^2 , \quad (1)$$

where σ_d is the spread due to the cells finite volume and σ_{TOF} represents the error in reporting the time-of-flight values. The latter is given by the error introduced by the "peak time" algorithm plus any spread due to variations in determining the hardware time offsets from run to run, as it will be explained next. The value of σ_d is not larger than 0.7 ns, which is given by the largest possible difference between the cells center distance d used in calculating $t_{TOF}^{\gamma} = d/c$ and the actual gamma-ray interactions distance. Thus, our time-of-flight measurement has an uncertainty of $1.3\ ns \lesssim \sigma_{TOF} \lesssim 1.5\ ns$.

Time-of-flight adjustments

When measuring time-of-flights of the order of few nanoseconds, even small mismatches in time delays among channels become important. Those differences in channel time delay can be easily observed in the

gamma-ray time-of-flight histograms for each cell pair as shifts from zero of the double Gaussian distributions, see Figure 37. Since channels within the same digitizer are synchronized with a common clock, time delay differences of few nanoseconds could still originate from hardware differences between the individual channels, like variations in the PMT response and in the cables length. In NSC's data collected at the SNS, the time shifts of each cell pair remained the same over a period of two years[1], as expected for time delays intrinsic to each channel hardware.

Though careful matching of the time delays should be attempted, it is not always possible to completely eliminate those differences in the hardware. Thus, to determine the individual channel time delays Δ_i, we make use of the following formula relating the measured and the real time-of-flight,

$$(t_{TOF})_{ij}^{measured} = \left(t_j^{real} + \Delta_j\right) - \left(t_i^{real} + \Delta_i\right) = t_{TOF}{}_{ij}^{real} + \Delta_{ij}\,, \quad (2)$$

where $\Delta_{ij} = \Delta_j - \Delta_i$, $i,j = (0,n)$ and $n+1=16$ is the number of channels in a given digitizer. The 120 off-diagonal values of Δ_{ij} are the shifts from zero of the double Gaussian fit of the gamma-ray time-of-flight histograms, as mentioned above. In practice, we only need to calculate 15 of them, for example Δ_{0i}, $i = (1,15)$, and solve for each channel time offset as $\Delta_i = \Delta_0 - \Delta_{0i}$. Since we only care about time differences between channels, the constant Δ_0 will always cancel out.

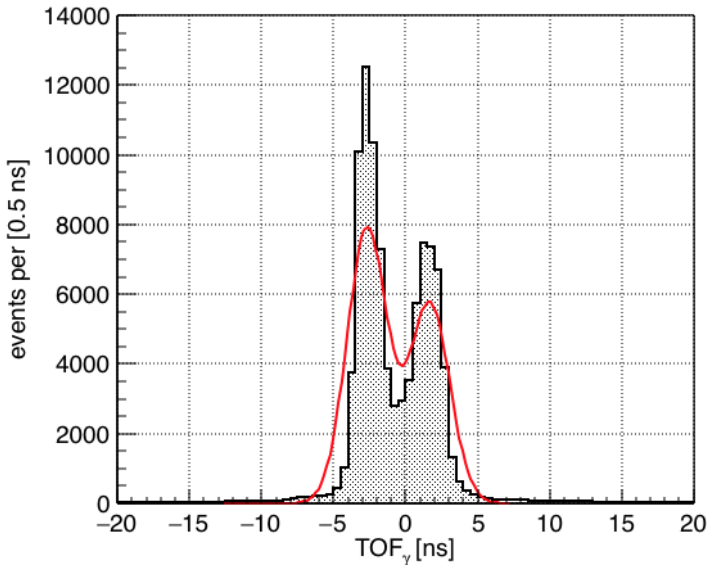

Figure 37: Histogram of the time between two consecutive gamma-ray interactions occurring in cell 7 (in the front plane) and cell 18 (in the back plane), after adjusting for individual channel time delays and inter-digitizer time offsets. The double Gaussian fit to the final histogram is shown in red, and has a standard deviation of about 1.5 ns on each peak.

A time offset between the two digitizers, which is locked at the beginning of each run when the digitizers timestamps are sequentially cleared to start the acquisition, also affects the current NSC data acquisition

[1] Only one channel time delay changed, probably due to hardware changes.

software. This inter-digitizer time offset—that can be in the tens of nanoseconds—only exits between channels of different digitizers: $\Delta_{ab} = -\Delta_{ba}$, where a,b = (0,1), $a \neq b$, are the digitizer indexes. As a consequence, the time-of-flight processing consists of two steps: first, calculate and apply the constant single channel time offset $\Delta_i = \Delta_0 - \Delta_{0i}$, and second, determine the inter-digitizer offsets $\Delta_{a_i a_j}$ for each run. The adjusted value of the time-of-flight, which should represent a better approximation of the real time-of-flight, is given by

$$(t_{TOF})_{ij}^{adjusted} = (t_{TOF})_{ij}^{measured} - (\Delta_{0i} - \Delta_{0j}) - \Delta_{a_i a_j}, \quad (3)$$

where a_i, a_j = (0,1), $a_i \neq a_j$, are the digitizer indexes of the corresponding channels i and j. The example of Figure 37 shows the results of shifting the measured *TOF* according to equation (3) for two channels of different digitizers. We find that, after adjusting the measured time-of-flight, offsets of about $1\,ns$ remain in $(t_{TOF})_{ij}^{adjusted}$, which introduce systematic errors in the final result.

Energy calibration

To calibrate each cell response over such large energy range, we combine the GEANT4 [5] Monte Carlo simulation of an isotropic flux of 1.46 MeV and 2.61 MeV gamma-rays representing ambient K^{40} and Th^{232} with a ray-tracing simulation of the muon spectra. The latter is obtained by sampling the muon direction from a $(\cos\theta)^2$ distribution [6], and approximating the muon deposited energy as 2 MeV/cm times the muon path length through the cell [13]. The simulated spectra are Gaussian smeared with an energy-dependent standard deviation

$$\sigma_E = \frac{E}{2.354}\sqrt{\epsilon_1^2 + \frac{\epsilon_2^2}{E} + \frac{\epsilon_3^2}{E^2}}, \quad (4)$$

where the constant values ϵ_1 = 0.30, ϵ_2 = 0.0013 MeVee^{½}, and ϵ_3 = 0.059 MeVee are averaged values previously measured for the NSC cells in the energy range 1 to 10 MeVee. For higher energies, equation (4) yields a 30 % energy resolution, which is worse than other values in the literature [15] for similar size cells. The resulting calibration of four example cells are shown in Figure 38.

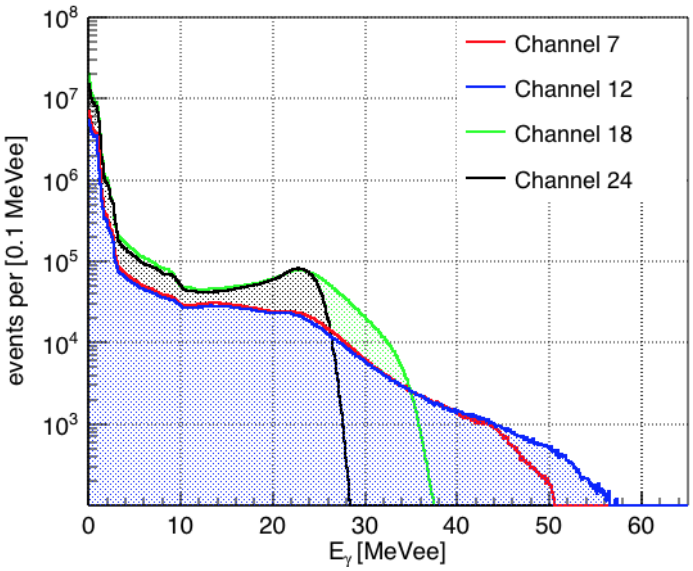

Figure 38: Calibrated spectra from gamma-rays and muon events of two front-plane cells (channel 7 and 12) and two back-plane cells (channels 18 and 24). Variations in the non-proportional channel response for large pulses cause the spectra endpoints to differ among all channels.

For the EJ-309 proton light-output response, we use the functional form and values proposed by Takada *et al*. [15], where proton energies from $E_{p\sim}$ 5 MeV up to $E_{p=}$ 70 MeV were measured with a cylindrical cell of dimensions similar to the NSC large cells. Since extrapolating the data from [15] to lower energies also falls within 25% of measured data in that range [16], we use the Takada *et al*. values across the full range of proton recoils energies.

PSD selection

The EJ-309 capabilities for differentiating gamma and neutron interactions via pulse shape discrimination (PSD) techniques has been extensively studied [17]. In this paper, we use a PSD parameter defined as the ratio of the integral of the full scintillation pulse, which includes both the fast and the slow components, over the integral of the initial fast scintillation component Figure 39 shows the histogram of the PSD parameter versus deposited energy E for an example channel from each plane from data collected at the SNS experimental hall during a 14-ms periodic window that is anti-coincident with the SNS's pulsed beam. The lower *gamma* PSD band, mainly due to gamma-ray and muon interactions (though we only call is "gamma band"), extends to about ~ 30 MeVee as expected. The higher *neutron* PSD band, produced mainly by proton recoils, also spans to the tens of MeVee due to the presence of intermediate-energy cosmic neutrons in the SNS experimental hall.

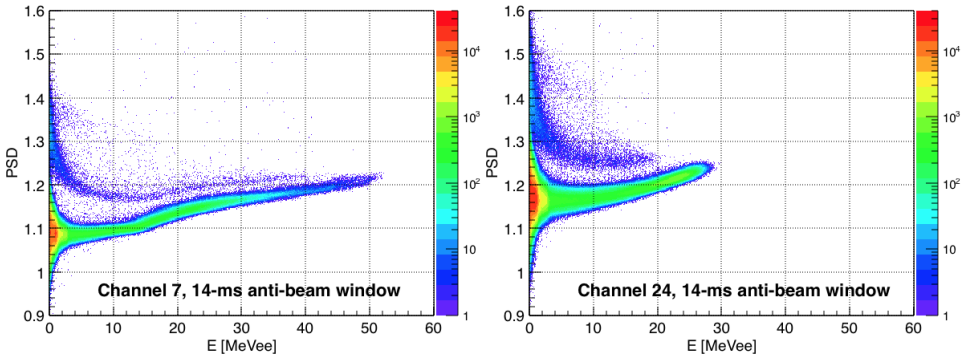

Figure 39: Histograms of the PSD vs. deposited energy E for a front-plane cell (channel 7) and a back-plane cell (channel 24) of data collected at the SNS experimental hall during a 14-ms window anti-coincident with the SNS's pulsed beam. As already pointed out in Figure 38, variations in the non-proportional channel response for large pulses cause the PSD bands endpoints to differ among channels.

Figure 40 shows the "PSD vs. E" histogram of the same data collected at the SNS experimental hall location, but restricted to a 1.3 μs beam-coincident window. In these data, the neutron PSD band produced by the beam-related intermediate-energy neutrons is considerably more populated compared to the cosmic neutron population of Figure 39, even though it corresponds to a factor of ~10^4 shorter measurement period. Another higher PSD band is clearly evident in Figure 40 data, and it is also present during the 14 ms anti-beam window data in Figure 39 though much fainter. This band corresponds to ionizing particles (deuterons, tritons, ^{3}He and α particles) resulting from neutron inelastic interactions with the carbon nuclei [18], but identification of the corresponding reaction channel is difficult due to the poor PSD resolution of these data.

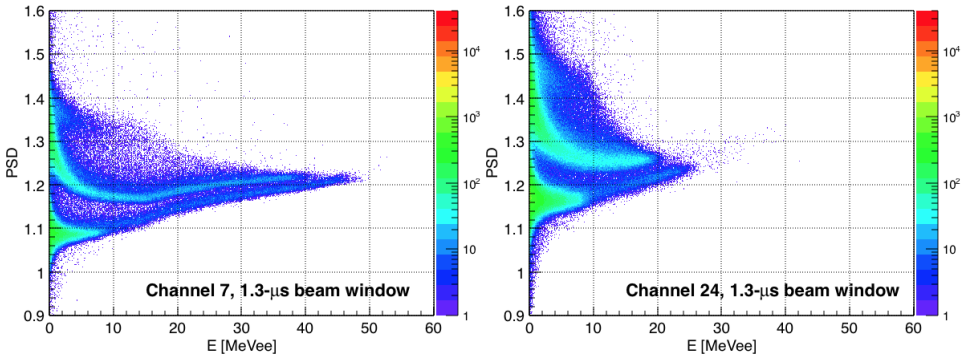

Figure 40: "PSD vs. E" histogram of data collected at the SNS experimental hall restricted to the 1.3-μs beam-coincident window of the SNS's 60-Hz pulsed beam. Comparing with the 14-ms anti-beam window histogram of Figure 39 show that most of the intermediate-energy neutron population is only present during the 1.3-μs beam-coincident window.

As it will be shown in the simulation section 4.1.2, recoiling protons produced by neutrons of more than ~50 MeV can be energetic enough to escape the NSC cells without depositing their entire kinetic energy in the cell. Such escaping protons will have a reduced slow scintillation component, and thus, a smaller PSD parameter than fully absorbed protons. We find compelling evidence suggesting that the lower PSD

band in the 1.3 μs beam window histograms of Figure 40 represents escaping protons created by the beam-related intermediate-energy neutrons. As a check, when restricting data to an anti-beam 1.3 us window, the total number of events in all bands drops by a factor of ~600, indicating that the lower PSD band during beam time is not due to a steady gamma-ray and muon background. Furthermore, Figure 41 shows that the lower PSD band during beam time is in average slightly higher in PSD values compared to the steady state gamma PSD band measured in anticoincidence with the beam. According to [18] and [19], escaping protons should precisely produce a PSD band between the gamma and muon induced electron band (a.k.a., the gamma PSD band) and the fully absorbed proton band (a.k.a., the neutron PSD band).

Nevertheless, the fact that the light-output E of the hypothesized escaping proton band extends beyond the maximum light-output observed for the fully absorbed proton band is puzzling, and prompts us to look for other physical explanation for that band. An arguable explanation for the appearance of an intense beam-coincident lower PSD band could be the presence of a high-rate beam-induced gamma flux. We have not completed a literature search to investigate whether such high-energy gammas (as high as ~25 MeVee) can be induced from intermediate to high energy neutron interactions. However, the presence of high-energy gammas will not explain by itself the upwards shift in the lower PSD band. Although it is conceivable that pulse pile-up due to a high-rate beam-induced gamma flux could increase PSD values, such upward shift would also affect the neutron PSD band, which is not observed in the SNS data. Thus, in what follows, we assume that such band actually contains the escaping proton population, and leave the understanding of its light-output features to future studies. Therefore, we also assume that the escaping protons are removed by the PSD cut so that the selected neutron population used in the image and spectrum reconstruction is not contaminated by scatter pairs where only a partial amount of energy was measured for the first scatter.

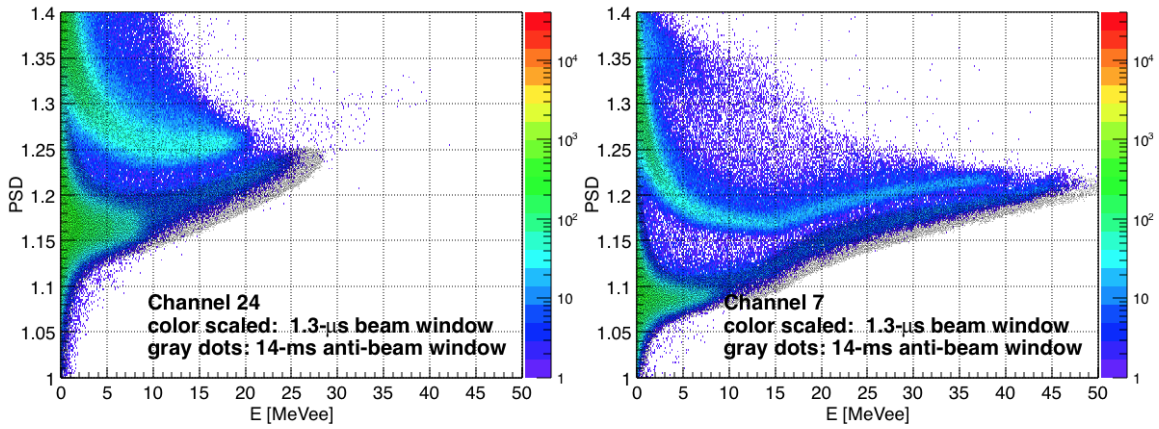

Figure 41: Superposition the "PSD vs. E" histograms of the 1.3-μs beam-coincident window data (show as a contour plot) and the 14-ms anti-beam window data (show as a gray shade) illustrating the upwards shift of the lower PSD band during beam time.

Separating the PSD bands over such large energy range and in the presence of a time-varying neutron flux characteristic of particle accelerators present practical challenges. For particle accelerators data, a

plausible strategy is to use the anti-beam data to determine the mean and width of the gamma band, while the neutron PSD band's mean and width are determined from the beam-related intermediate-energy neutrons that show up only during the beam-coincident time window. However, the optimal neutron-gamma PSD boundary that maximizes neutron acceptance and gamma rejection depends on the relative size of the neutron and gamma populations [20] and should in principle be determined for each time-windowed dataset. An obvious complication is the presence of an escaping proton band that should also be excluded. Setting the PSD boundary according to particles' relative population becomes even more important at low light-output where the various species bands start overlapping, but is also relevant when the intermediate-energy neutron population is highly suppressed due to, e.g., the presence of heavy concrete shielding or overburden. Moreover, a neutron-alpha boundary to exclude alpha events from the neutron selection should also be drawn according to the population of the two particle types. In practice, however, due to the large differences in the various particle populations for each time-windowed dataset, it might only be possible to calculate fixed boundaries, as in the examples shown in Figure 42.

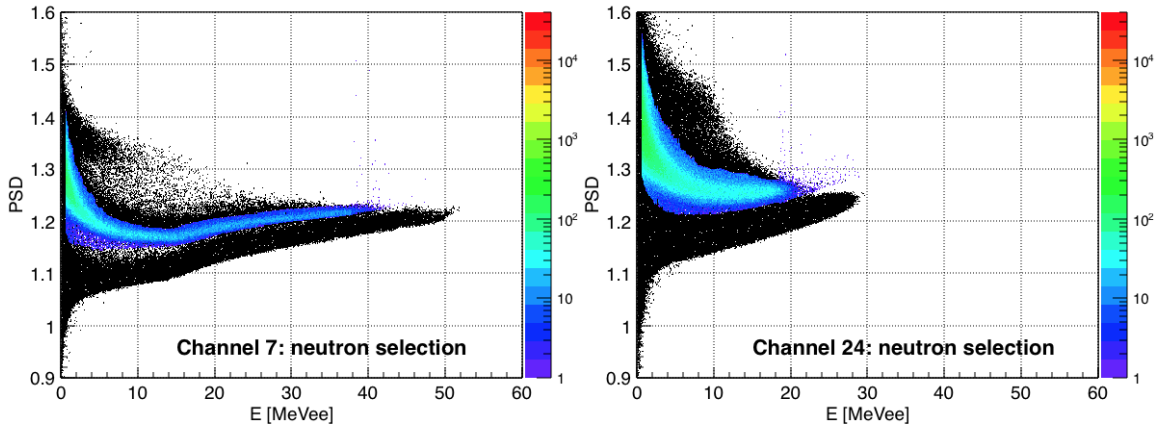

Figure 42: Examples of neutron PSD selection along the full energy range, where the events in black have been rejected as non-neutron events. The lower neutron boundary has been obtained from and energy-dependent double Gaussian fit [21]. The upper neutron boundary to exclude alpha events has been set to 4 times the neutron-band Gaussian standard deviation above the Gaussian mean.

In this data, we found that cable reflections due to impedance mismatch produces a bend in the PSD bands when the negative reflections of large signal pulses are clipped off at the bottom of the digitizer's dynamic range. While this could be prevented by proper impedance termination, it constitutes another example of practical issues due to accepting a larger range of pulse amplitudes that further complicates the PSD boundary calculation.

4.1.1.3. Source Reconstruction

Another modification to the NSC data analysis required for intermediate neutron energies is the use of the relativistic formula for the kinetic energy term of equation $E_n = E_0 + E_{n'}(d, t_{TOF})$, given by

$$E_{n'}(d,TOF) = mc^2\left[\frac{1}{\sqrt{1-\frac{1}{c^2}\left(\frac{d}{t_{TOF}}\right)^2}}-1\right] \quad (5)$$

Consequently, a lower time-of-flight bound corresponding to the gamma-ray time-of-flight $t_{TOF}^{\gamma} = d/c$ between the cells centers should be imposed when selecting candidate neutron pairs. Figure 43 shows two E_n histogram examples corresponding to SNS data restricted to the 1.3 μs beam-coincident window (when the intermediate-energy neutrons are present) and to data during a 14 ms window anti-coincident with the SNS's pulsed beam. Though very different in rate, both reconstructed neutron spectra present similar shapes. As it will be shown in the next section, this is mainly due to the strong degradation in the NSC spectroscopic capabilities at these higher energies.

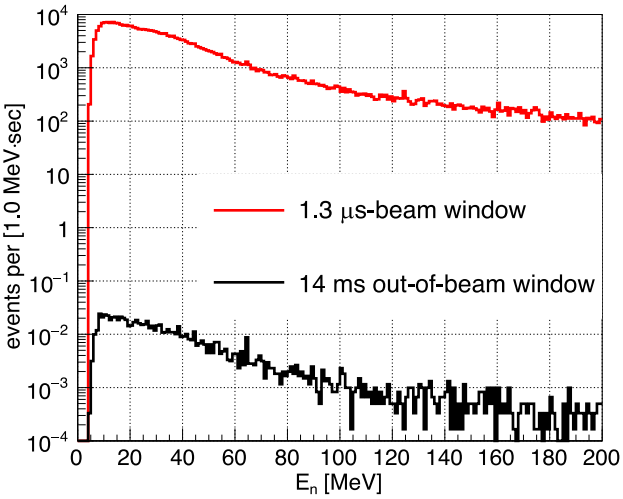

Figure 43: Histogram of the neutron reconstructed energy E_n for the 1.3 μs beam-coincident window and a 14 ms window anti-coincident with the SNS's 60-Hz pulsed beam.

The relativistic formula of the scattering angle still depends on E_n and E_0:

$$\cos\theta = \frac{p_{n'} + q\cos\alpha}{p_n} \quad (6)$$

where p_n and $p_{n'}$ are the magnitudes of the incoming and scattered neutron momenta, and

$$q\cos\alpha = \frac{E_n E_{n'} + E_0\left(M_n c^2 - M_p c^2\right)}{p_{n'}} \quad (7)$$

is the projection of the proton recoil momentum along the scattered neutron direction, with $M_n c^2$ and $M_p c^2$ being the neutron and proton rest mass energies.

The neutron source image is currently generated using the superposition of back-projected neutron direction cones. Double scatter events occurring in any pair of cells, irrespective of their planes, are accepted in order to increase efficiency. To account for the instrument's non-uniform angular response, images produced in the presence of a directional source (e.g., during the 1.3 μs beam-coincident window) are normalized by the "background" spectra collected in the absence of the source (e.g., during the 14 ms anti-beam window). Such an efficiency normalization of the back-projection image is only exactly valid under a uniform, energy-independent, neutron background, which is not the case at the SNS experimental hall, where the concrete beamline walls can exacerbate non-uniformities in the cosmic neutron background. Figure 44 shows the normalized NSC images for the fast reconstructed-energy range $E_n = \sim 0, 10\ MeV$, where most of the neutrons are imaged as arriving from the direction where the SNS target was located. One the other hand, when restricting to the intermediate reconstructed-energy range $E_n = 10, 50\ MeV$, the normalized NSC image is highly degraded and does not show the direction of the intermediate energy neutrons as mainly arriving from the SNS target location.

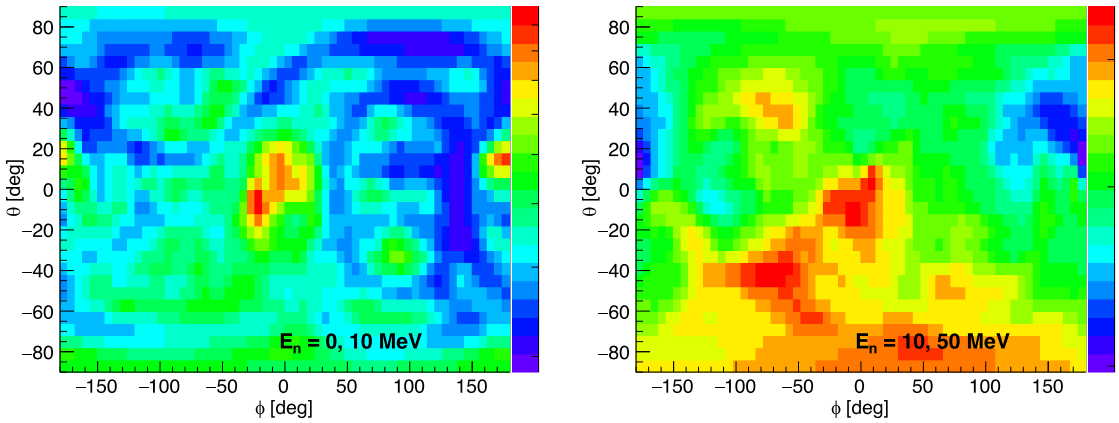

Figure 44: NSC back-projection images covering reconstructed energies in the fast range $E_n = \sim 0, 10\ MeV$ (left) and in the intermediate range $E_n = 10, 50\ MeV$ (right). The SNS target direction is at the center of the image.

The NSC response has been extensively modeled in the fast-neutron energy range 1-10 MeV [10], allowing the application of inverse methods for spectrum and image reconstruction like the Maximum Likelihood Expectation Maximization (MLEM) [22] algorithm. For energies beyond 10 MeV, scatters in carbon nuclei become relevant, including several inelastic channels producing protons, alphas, Be and other recoiling isotopes [24]. In contrast to the fast-neutrons response map, which can be approximated using a simplified pseudo-Monte Carlo interaction probability code [25] [26], the complexity of the neutron interaction channels at higher energies requires the use of a full Monte Carlo interaction package. The latter approach, though in principle tractable, is intrinsically computational intensive in order to achieve acceptable variance for all the response map spatial pixels. Furthermore, as we address in the next section, such simulated intermediate-energy neutron response would require careful and difficult experimental validation.

4.1.2. Instrument Limits

In this section, we focus on simulating a subset of representative incoming neutron energies with the goal of gaining insight on how the NSC response changes as the neutron energy increases. For that purpose, we built a GEANT4-based [2] Monte Carlo model of the NSC. For energies below 20 MeV, the GEANT4 tool-kit provides data-driven high precision hadronic models. However, the physical models for neutron interaction above 20 MeV are typically not data driven but based on parametrical or theoretical hadron interactions models. Of the GEANT4 ready-to-use physics modules, we chose the QGSP_BERT_HP physics list. While benchmarking the simulated NSC response is possible with laboratory neutron sources up to about 14 MeV, doing so is not straightforward beyond this energy due to lack of easily available and well characterized intermediate-energy neutron sources. Nevertheless, the simulation results presented in this section are useful for the purpose of understanding response features that are generally due to the intermediate-energy neutron interactions in the NSC, even if the resultant interaction rates cannot be benchmarked.

Our simulated model includes the front and back NSC planes, each comprising 16 aluminum cells of 0.5 cm width containing EJ309 liquid scintillator, with an acrylic window at the cells' side external to the instrument. The model does not include the PMTs, the holding frames or any of the electronics. Though the results presented below correspond to using air as the world material, using vacuum instead did not significantly change the simulation outcome. All the dimensions and physical parameters take the same values described in the above sections for the actual NSC instrument. The simulated incoming neutron field corresponds to a plane wave incident on the front plane with direction perpendicular to the NSC planes. To save computational time, the neutrons start positions were uniformly sampled only on the external faces of the 16 front cells. One million neutrons were generated for each of the simulated energies $E_{pw} = 2, 5, 10, 50, 100, 150, 200\ MeV$.

In simulation data, we form double-scatter neutron events only with proton tracks created in different cells within a coincident window set to 100 ns. We assume that ionization tracks created by other ionizing particles, like electrons, alpha particles, Carbon ions, etc.., would be eliminated in real data by pulse shape discrimination. This assumption is obviously an approximation, especially at low deposited energies where the PSD bands of the various ionizing particles overlap. Following the assumption that escaping protons can be identified by pulse shape discrimination (see section 4.1.1.2), we also reject proton tracks that escape the scintillator material with 1 MeV of kinetic energy or more. Since protons recoiling in organic scintillators reach their maximum rate of energy loss at just below 1 MeV of kinetic energy [23], those that escape the scintillation material with more energy should produce a reduced slow scintillation component—and PSD value—compared to fully absorbed protons of the same initial energy. Figure 45 shows the histogram of the protons' final kinetic energy in all of the NSC cells for an incident neutron plane wave energy $E_{pw} = 100\ MeV$, in which case, about 8% of all the produced protons leave the scintillator material with more than 1 MeV of energy.

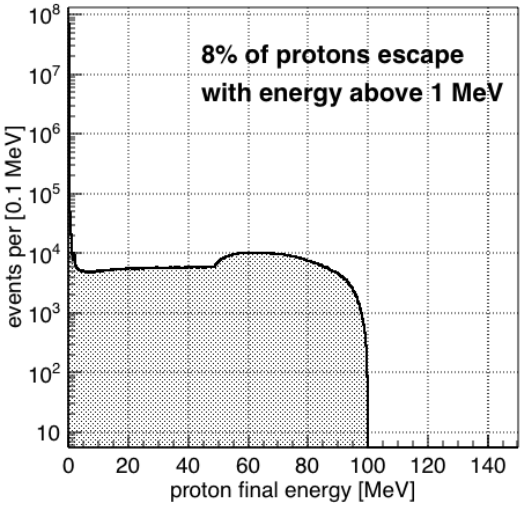

Figure 45: Histogram of the protons' final kinetic energy in the scintillator material for incident neutrons with energy E_n = 100 MeV. About 8 % of all the protons tracks leave the scintillator material with more than 1 MeV of energy.

For each non-escaping proton track, we record the total deposited energy, the start time and position within the cell, and the particle responsible for creating the proton track. The total energy deposited by a proton track in a given cell is converted into light-output "MeVee" units using data from [15]. This light-output energy should then be Gaussian smeared with the energy-dependent standard deviation given by equation (4) in order to account for the experimentally measured energy resolution, and to properly apply the experimental energy threshold on the smeared light-output. However, in order to isolate response features due to the interactions dynamics and the instrument geometry, we first analyze the histograms of the reconstructed neutron energy $E_n = E_0 + E_{n'}(d, t_{TOF})$ without folding in the experimental errors in measuring the energy, time and position of the scatters. When computing the *exact* E_n, the energy deposited by the first proton recoil of the pair, E_0, is directly extracted from the simulation values without applying any resolution smearing, and the kinetic energy $E_{n'}$ is calculated using the exact values of time and position of the two proton recoils to respectively get the t_{TOF} and d of formula (5).

We select the plane wave energy $E_{pw} = 100\ MeV$ to highlight several NSC response features directly associated with intermediate neutron energies. Figure 46 shows the *exact* E_n histogram where the proton-track pairs are formed by the first two proton tracks of each simulated event that occur in different cells, applying a zero-energy threshold and selecting only those tracks whose generating particle was the primary neutron of the simulated event. Although these are restrictive selection conditions not attainable experimentally, they help to make the expected neutron reconstructed energy peak at 100 MeV clearly evident. Reconstructed neutron energies outside the 100 MeV peak are the result of applying a zero-energy threshold to the Gaussian smeared light-output, and thus, of eliminating proton tracks resulting in a negative smeared light-output. In those cases, the neutron pairs are formed by the next consecutive proton tracks produced by the primary neutrons, which do not reconstruct the value E_n = 100 MeV. Although proton tracks with negative smeared light-output are an artefact of our simulation processing

Gaussian smearing, they are equivalent to very low values of light-output due to the scintillator's poor energy resolution, that would be eliminated by a realistic nonzero threshold. We choose to include those events in Figure 46 because doing so will facilitate the understanding of the E_n histograms below, where the neutron pair selection conditions are gradually relaxed to more realistic ones.

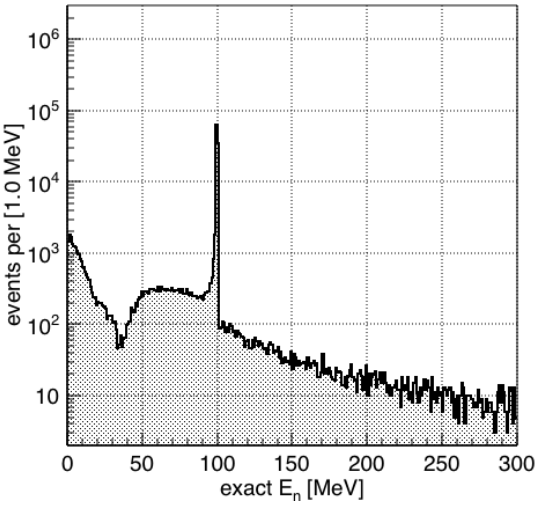

Figure 46: Histogram of the exact E_n for the simulated incoming neutron plane wave with energy $E_{pw} = 100\ MeV$. Event pairs are formed only by the first two proton tracks generated by the primary neutron. The number of incident neutrons was 10^9. See text for other important details.

A more realistic representation of the NSC data event selection is obtained by lifting the restriction that the proton tracks are generated by the primary neutron and by including all possible proton-track pairs of the event that still satisfy the 100-ns coincidence window. Moreover, we combine into one "track" those proton recoils within the same cell taking place consecutively in a 10-ns pile-up window (about the rise time of EJ309 scintillator pulses) by summing their energies and assigning to the new track the time and position of the first of the combined recoils. Also, a 0.5 MeVee threshold is applied to the tracks Gaussian smeared light-output, though the exact value of the deposited energy E_0 is still used in calculating the *exact* E_n. The histograms resulting from gradually applying these pair selection conditions, presented in Figure 47, show the 100 MeV peak containing the correct proton-track pairs due to the first two elastic scatters of the primary neutron. In the final histogram, shown in black in Figure 47, a population of contamination proton-track pairs due to other processes still dominates the response at low and high values of reconstructed energy E_n. Besides the effect of smeared light-output threshold discussed in the previous paragraph, other processes spreading the *exact* E_n response originate from neutron multiple elastic scatters and from neutron inelastic interactions that create other secondary neutrons and protons. Also, escaping protons with more than ~ 50 MeV will have sufficient energy to traverse the 0.5 cm aluminum cell walls and produce a neutron-like scatter if fully absorbed in another cell [23].

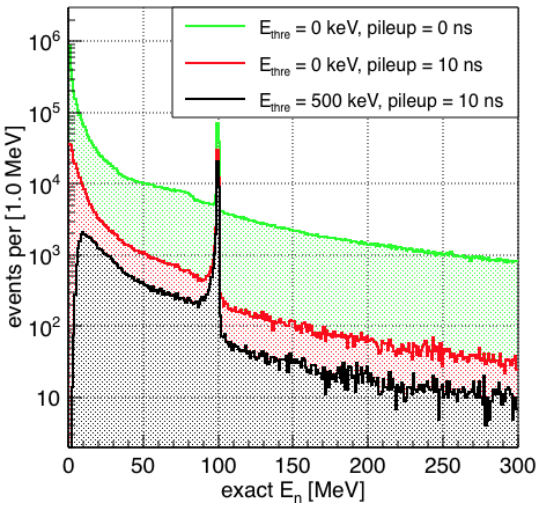

Figure 47: Histogram of the exact E_n for the simulated incoming neutron plane wave with energy $E_{pw} = 100\ MeV$. The selection of event pairs is according to more realistic representation of the NSC data event selection. The number of incident neutrons was 10^9. See text for other important details.

The measured response contains the experimental uncertainties in the deposited energy, the time-of-flight and the interactions distance. In Figure 48, the effect of separately introducing each of those uncertainties in the calculation of E_n is compared. As indicated above, the deposited energy is first converted to light-output, then it is Gaussian smeared and converted back to energy units. The pair's t_{TOF} is also Gaussian smeared with $\sigma_t = 1.5\ ns$. For the interactions distance *d*, the fixed separation between the cell's centers is used as it is done in experimental data.

Including the uncertainty in E_0 or t_{TOF} creates large tails in the higher energy bins. Scatter pairs with large energy depositions in the first cell are the ones mainly contributing to the tail when E_0 is smeared. On the other hand, energetic scattered neutrons with short t_{TOF} relative to σ_t are the ones contributing to the histogram tail when the t_{TOF} is smeared. Note also that separately smearing the energy E_0 and t_{TOF} still leaves in each case a small but well defined peak at 100 MeV, confirming the presence of these two opposite populations of *correct* double-scatter events: one where most of the incident neutron energy goes into the scattered neutron (and thus E_n is nearly unchanged when smearing small E_0 values) and one where most of the energy goes into the recoiling proton (and thus E_n is nearly unchanged when smearing long t_{TOF} values). The separation into mainly two populations is a geometrical effect particular to our plane wave simulation, since neutrons scattered with medium angles leave the NSC without encountering a second cell. However, it is still useful to contrast the effect of the uncertainty in E_0 or t_{TOF} with the effect of using the fixed distance between cells. The latter case results in larger E_n smearing when the uncertainties in E_0 or t_{TOF} have a relatively small effect, and thus the peak at $E_n = 100\ MeV$ is highly spread. On the other hand, using the fixed cells distance creates a smaller tail at higher energies.

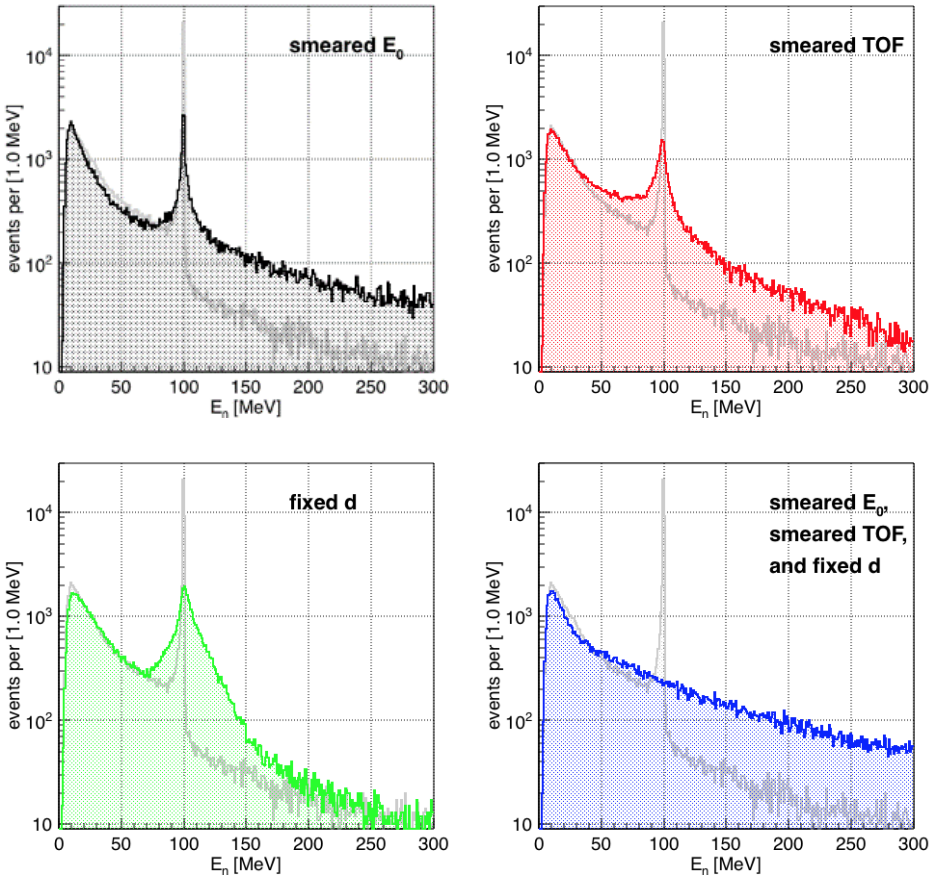

Figure 48: Effect of separately smearing each of measured experimental quantity entering in the calculation of E_n. The number of incident neutrons was 10^9.

The final *exact* E_n histogram of the $E_{pw} = 100\ MeV$ plane wave, with all the uncertainties included, is shown in the last plot of Figure 48. It corresponds to a wide distribution that slowly decays with energy and extends to values much higher than 100 MeV. Therefore, the current uncertainty values in measuring E_0, t_{TOF} and d represent the intrinsic limit to the NSC response at these high neutron energies.

Finally, the left pane of Figure 49 compares the exact E_n histograms for all simulated plane wave neutron energies and the right pane presents the corresponding smeared E_n histograms. The later histograms suggest that information identifying original incoming neutron energies above ~ 100 MeV is basically lost due to the measurement uncertainties of the current NSC. Although the simulated GEANT4 model has not been validated with data, these results indicate that unfolding source neutron energies above ~ 100 MeV would not be possible due to response degeneracy for those energies. Nevertheless, the presence of a relatively high event count for $E_n > \sim 50\ MeV$ might be used as evidence of the presence of an intermediate-energy neutron flux.

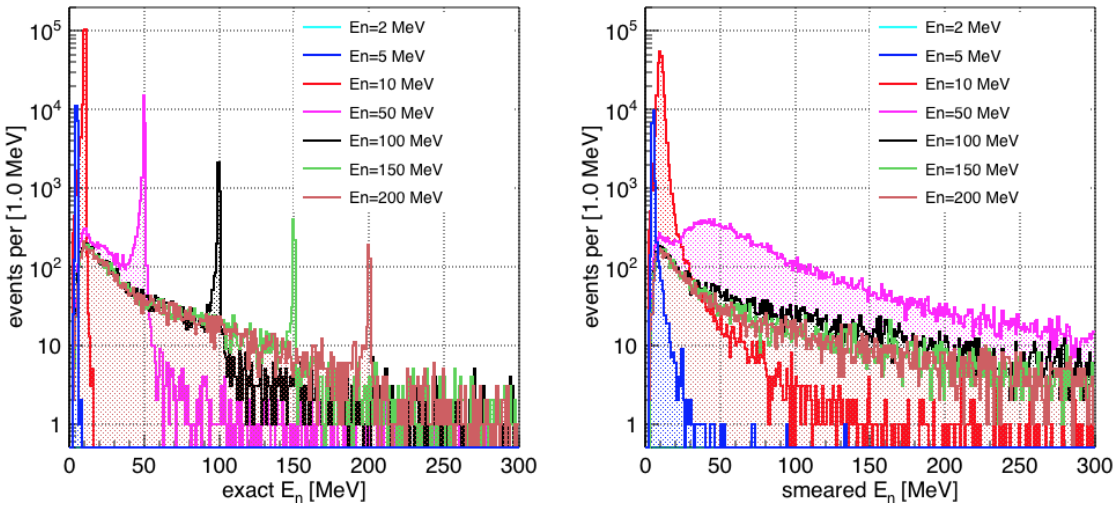

Figure 49: The histograms of the exact E_n (left) and of the smeared E_n (right) for all simulated neutron plane wave energies. The number of incident neutrons per simulated plane wave energy was 10^8.

4.2. Neutron Background Measurements at SNS

4.2.1. Overview of data collection campaign

The NSC data collection campaign at SNS comprised five measured locations over the course of three years. The SNS experimental hall blueprints in Figure 50 show the two locations labeled as "beamline 8" and "beamline 14a" according to their proximity to SNS beamlines. The three measured basement locations are shown in Figure 51, and are labeled as "basement C2.5", "basement C4" and "basement C11" according to their proximity to basement wall postings. Table 2 contains the chronology of the data collection periods per location and beam status. Data was also collected in each location during beam-off periods to measure the steady-state background baseline. The NSC measurement schedule was based on the SNS beam-on schedule, location availability and SNS personnel and local ORNL colleagues' availability to move and deploy the NSC. The sequence in measured locations, however, was also determined from the data analysis results for each dataset. For example, the initially measured beamline 14a show significantly large beam-related neutron background which prompted to move the next round of measurement to the better shielded SNS basement.

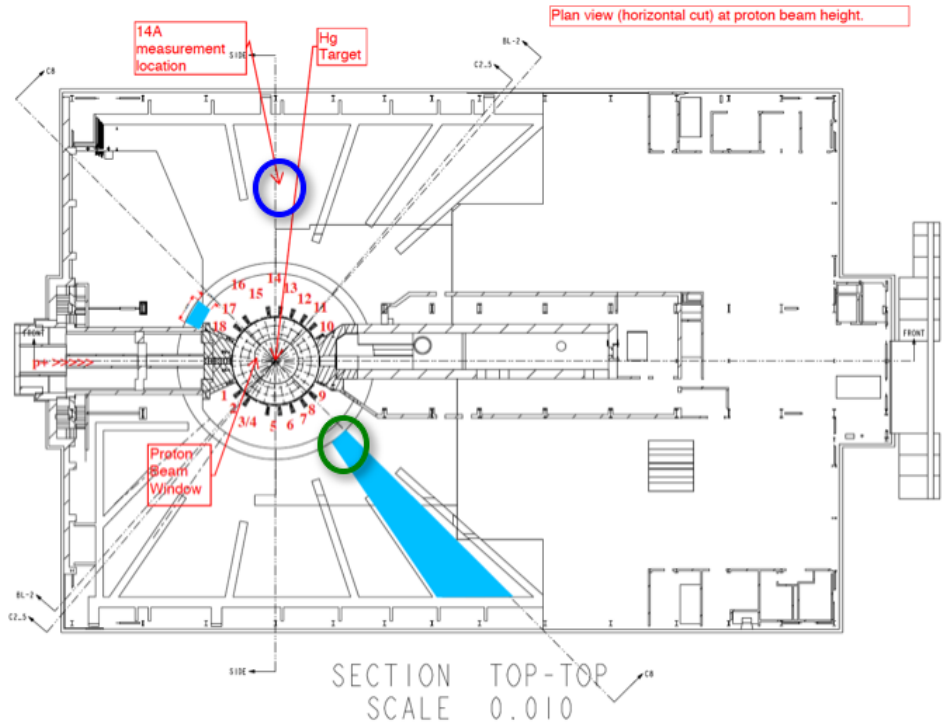

Figure 50: Measurement locations at the SNS Experimental Hall: beamline 14a indicated with a blue circle and beamline 8 indicated with a green circle. Blue print is courtesy of ORNL collaborators.

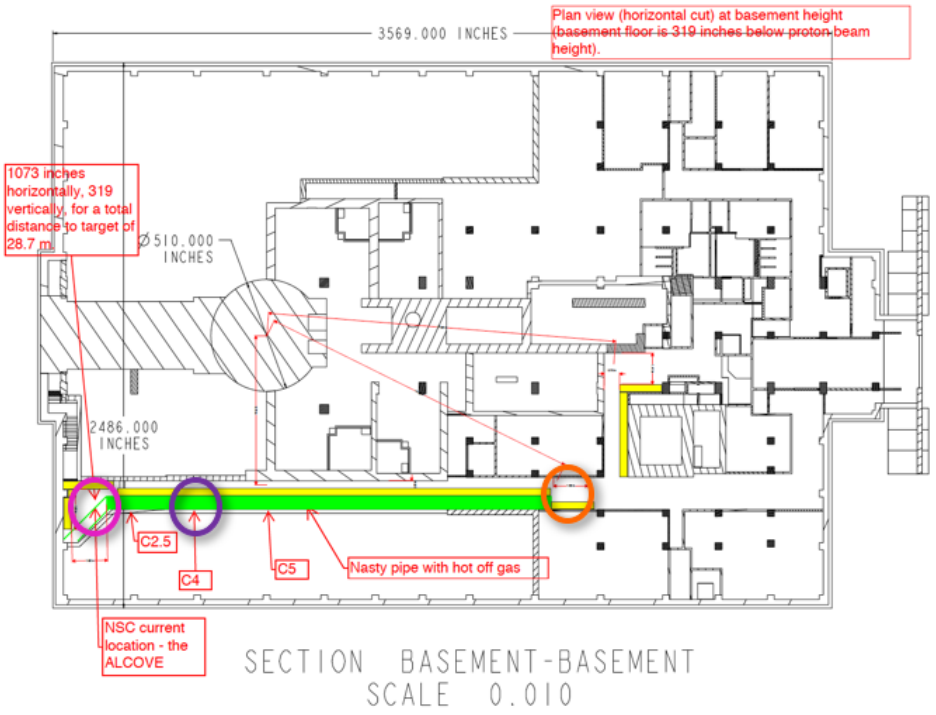

Figure 51: Measurement locations at the SNS basement: C2.5 indicated with a pink circle, C4 indicated with a purple circle and C11 indicated with an orange circle. Blue print is courtesy of ORNL collaborators.

SNS Location	Start Date	End Date	Beam Status
Beamline 14a	8/15/2013	9/29/2023	**ON**
	9/30/2013	10/3/2013	**OFF**
	10/29/2013	12/6/2013	**ON**
Basement C2.5	6/20/2014	6/25/2014	**ON**
Basement C11	9/18/2014	10/18/2014	**OFF**
	10/21/2014	10/27/2014	**ON**
	10/28/2014	11/18/2014	**OFF**
	11/19/2014	12/21/2014	**ON**
	1/8/2015	1/16/2015	**OFF**
	1/17/2015	2/18/2015	**ON**
Beamline 8	4/6/2015	4/11/2015	**ON**
	4/12/2015	4/19/2015	**OFF**
	4/20/2015	5/27/2015	**ON**
Basement C4	9/2/2015	09/26/2015	**ON**
	9/26/2015	10/8/2015	**OFF**
	10/9/2015	12/23/2015	**ON**
	2/6/2016	3/22/2016	**ON**
	3/23/2016	3/29/2016	**OFF**
	3/30/2016	5/11/2016	**ON**

Table 2. Chronological time table of NSC data collection periods at the SNS from 2013 to 2016. The beam level varies across the beam ON periods (see beam power plots below). Most data periods contain short interruptions due to hardware issues.

The NSC continually collected one-hour (or two-hour) data files during the whole measurement campaign. Although timing signals of the 60-Hz pulsed beam were available, collecting data continuously allowed us to determine the correct timing of the pulsed-beam "windows" by the increase the neutron rate, as shown in Figure 52. This figure shows the "time-to-trigger" histograms for two measured SNS locations of the NSC events timestamp with respect to the SNS-provided beam timing signal, here called "trigger". As such, the horizontal axis extend to 1/(60 Hz) ≅ 16.667 ms.

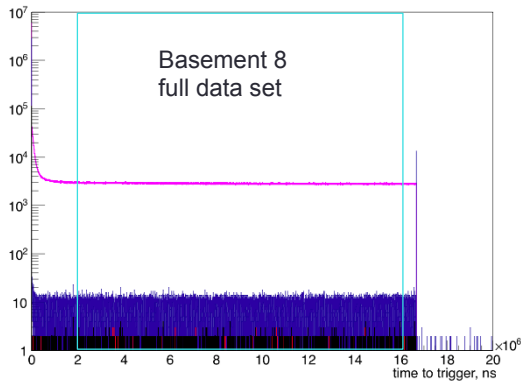

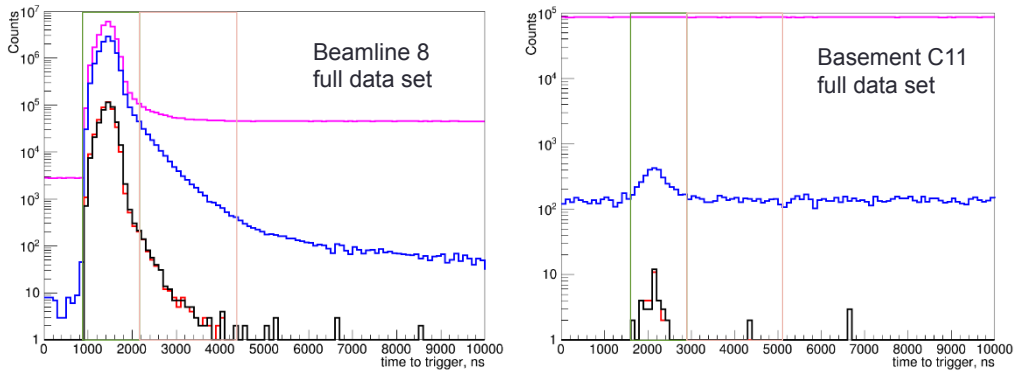

Figure 52: Time-to-Trigger histograms for two measured SNS locations. Pink line: all NSC detected events; blue line: PSD-selected neutron events; red and black lines: first and second neutron events forming a NSC neutron pair. The top histogram shows the full range from 0 to ~16.667 ms, while the bottom histograms have been zoomed down to show the event distributions during the beam windows for each dataset. Continuously collecting data reveals differences in the beam time offset with respect to the SNS-provided timing signal among different locations.

The data collected on the SNS experimental hall (Figure 52, left and middle histograms) indicate that the beam-related neutrons mostly show up during a 1.3 μs "prompt" window (green shaded in Figure 52), also called beam extraction window, that is coincident with the protons-on-target (POT) and the emission of the prompt ν_μ. The beam-related neutron rate is significantly reduced during a posterior 2.2 μs "delayed" window (orange shaded in Figure 52), when the ν_e and $\bar{\nu}_\mu$ from muon decay are emitted. A third 14-ms window (cyan shaded in Figure 52), that is anti-coincident with the beam, was used to measure the steady background during beam-on periods. Therefore, the data was separated in three 60-Hz-pulsed time windows: the 1.3-μs prompt window, the 2.2-μs delayed window and the 14-ms anti-beam window.

For each measured location and period, we plot the SNS beam power level in Joules per second for each sequentially collected data file. These plots reveal the hourly variation in beam power even during nominal beam-on periods, which subsequently change the beam-related neutron flux. Therefore, the neutron rates reported in section 4.2.2 for each location are normalized the total beam power during beam-on periods.

4.2.2. Datasets per Location

4.2.2.1 Beamline 14a

We started the measurement campaign at the beamline 14a location situated on the SNS experimental hall since this was the first available location close to the SNS target and suitable to hold the future experimental systems. The NSC was placed about 22 meters from the SNS target within a wedge delimited by the concrete walls of beamlines 13 and 14, as shown in Figure 53, with the thinner cells closer to the target. The more important finding in this location is that a beam-related high-energy neutron rate, too intense for a successful CNNS experiment, are able to traverse the concrete walls shielding the SNS target. Being on ground level, beamline 14a has negligible building overburden for the cosmic

neutron flux, but this steady-state background is at least 6 orders of magnitude smaller than the beam-related neutrons.

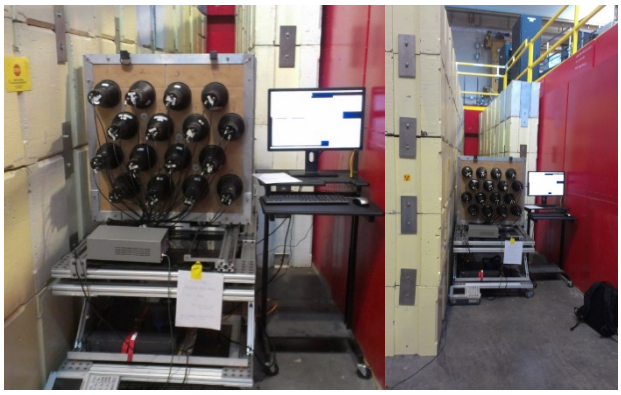

Figure 53: NSC at beamline 14a.

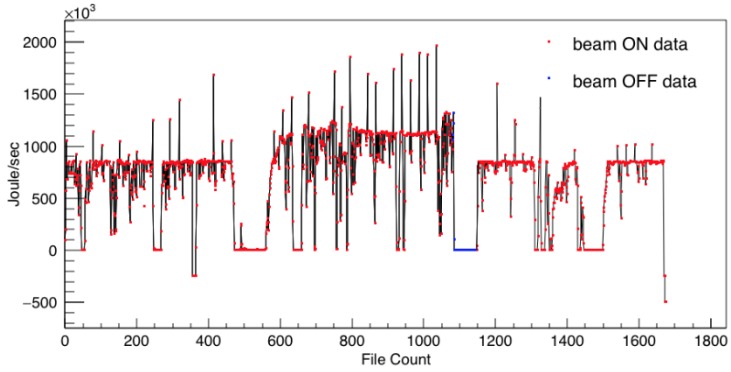

Figure 54: SNS beam power for each data file collected at beamline 14a. Beam power data courtesy of SNS.

4.2.2.2. Basement C2.5

The NSC was moved to the SNS basement, which is shielded by a high-density concrete monolith from the mercury target. The instrument then collected data for a brief period in an alcove at the end of the basement hall and next to a stairwell. One reason this dataset is so short was that part of the data was discarded due to a high gamma-ray background present in basement C2.5 that produced an elevated trigger rate and data acquisition dead time. It was discovered that an intense 511-keV gamma-ray flux was emitted during beam operation from a target exhaust line attached to the basement wall. As result, the thresholds of NSC individual channels were raised.

Nevertheless, there were important finding in this location. First, we discovered that the beam-related high-energy neutron flux is attenuated by 5 orders of magnitude with respect to beamline 14a (Figure 70). Furthermore, the NSC image suggested that the few beam-related high-energy neutron events recorded during the 1.3 μs prompt windows seemed to be coming from the stairwell, where the concrete shielding is obviously weaker. The increased overburden at basement C2.5 to about 8 m.w.e. reduced the steady-state cosmic neutron rate by more than one order of magnitude with respect to beamline 14a.

Figure 55: NSC at the basement C2.5 alcove.

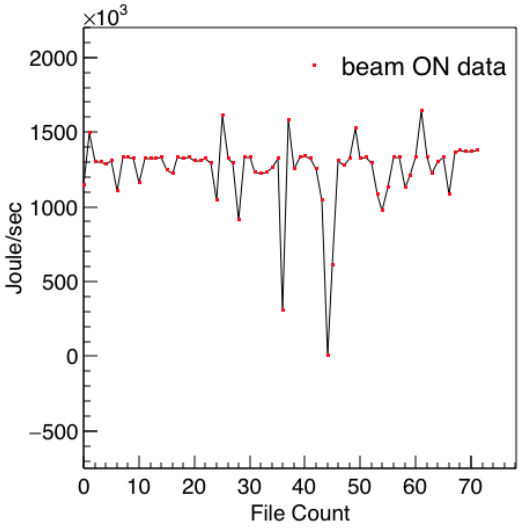

Figure 56: SNS beam power for each data file collected at basement C2.5. Beam power data courtesy of SNS.

4.2.2.3. Basement C11

Based on the findings in basement C2.5, it was decided to move the NSC to basement C11, which is a more spacious basement location that would facilitate the deployment of more than one detector system but still provide shielding against SNS target neutrons. This location was not found to be affected by the high gamma-ray background of basement C2.5, see section 4.2.2.5 for more details. Since this location has only 0.5 m.w.e. of overburden, the steady-state neutron background increased by nearly one order of magnitude higher than at basement C2.5. The beam-related neutron rates in this location were found to be nearly equivalent to those at basement C2.5 (Figure 70). Nevertheless, basement C11 has currently been ruled out by the COHERENT collaboration as a candidate location for a Ge system deployment because it is too far from the SNS target (~38 meters) to achieve an acceptable signal-to-background ratio with the currently available Ge mass.

Figure 57: NSC at basement C11.

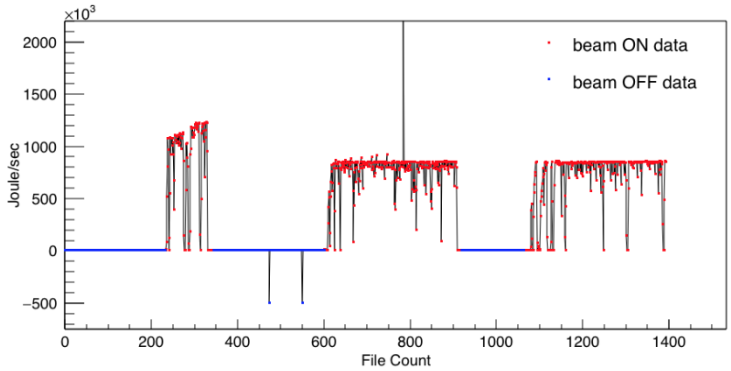

Figure 58: SNS beam power for each data file collected at basement C11. Beam power data courtesy of SNS.

4.2.2.4. Beamline 8

Motivated by the proximity to the SNS target at beamline 8—about 15 meters—, NSC data was collected at this other experimental hall location. However, we found beam-related neutron rates similar to those measured at beamline 14a (Figure 70), which still prohibit a successful CNNS detection even at this closer distance range.

Figure 59: NSC at beamline 8.

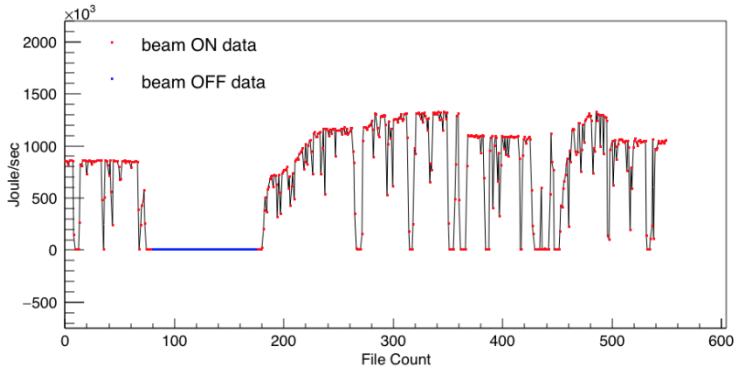

Figure 60: SNS beam power for each data file collected at beamline 8. Beam power data courtesy of SNS.

4.2.2.5. Basement C4

Basement C4 has been selected by the COHERENT collaboration as the main candidate for the deployment of their Ge system since it is the basement location closest to the SNS target—about 22 meters. Conveniently, our NSC measurements have shown that basement C4 has the lowest beam-related neutron rates, in both the 1.3-μs prompt window and in the 2.2-μs delayed window, compared to all other measured locations, see Figure 70. The steady neutron background rate at basement C4 is lower than the rate at basement C2.5, see Figure 72, revealing unexpected difference in overburden between the two locations. Moreover, the apparently lower beam-related neutron rates at basement C4 compared to the basement C2.5 alcove rates also represented an interested result since both location were assumed to be similarly shielded from the SNS target. Though more basement C2.5 data would be necessary for a conclusive result, it might be possible that the stairwell next to the basement C2.5 alcove is responsible for an increased beam-related neutron rate.


Figure 61: Basement C4 before NSC deployment.

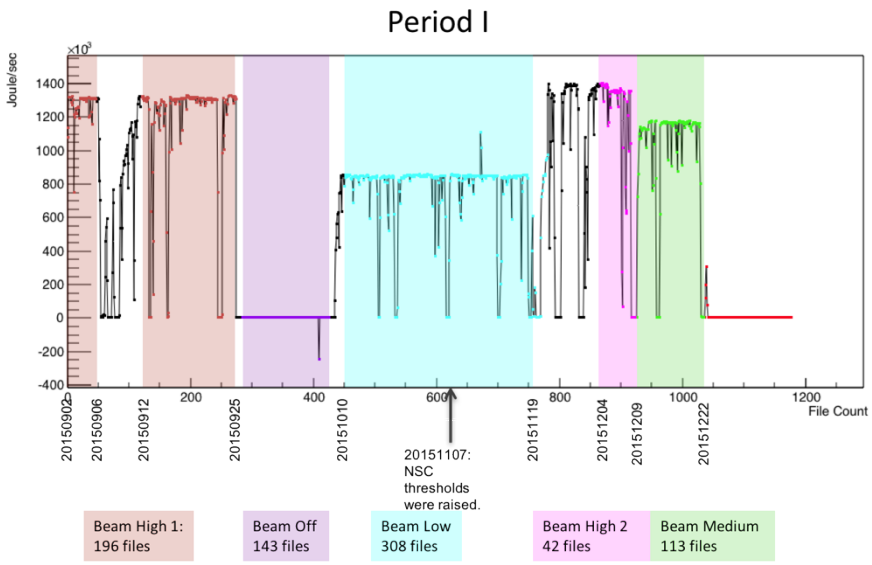

Figure 62: SNS beam power for each data file during the first data collection period collected at basement C4. Beam power data courtesy of SNS.

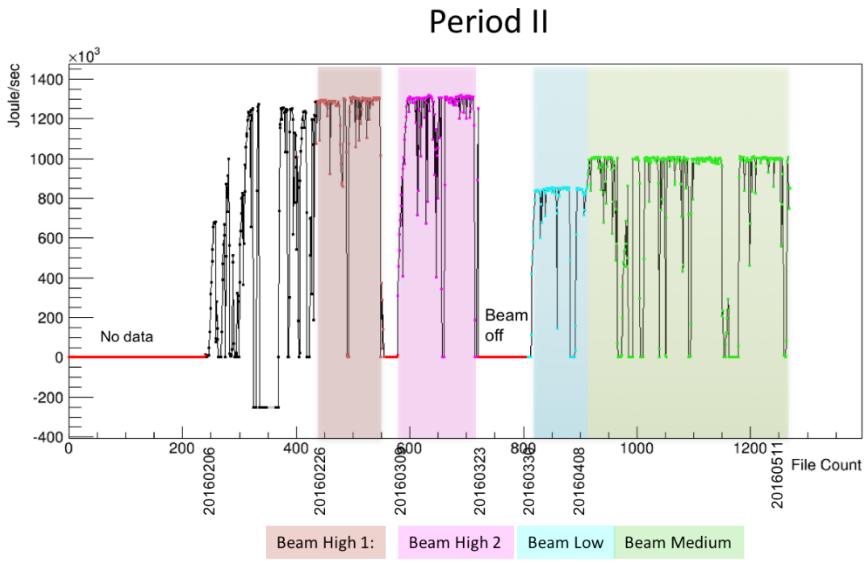

Figure 63: SNS beam power for each data file during the second data collection period collected at basement C4. Beam power data courtesy of SNS.

Basement C4 is also affected by the elevated 511-keV gamma-ray background emitted by the target exhaust line during beam operation. Though raising the NSC individual channel thresholds to just above 511 keV already reduces the hardware dead time to an acceptable rate, we found evidence that the gamma-ray background is producing piled-up pulses at high rate. Figure 64 compares the PSD vs. deposited energy E (in "adc" units) between the beamline 8 data and all the measured basement locations. Since beamline 8 was not affected by the high gamma-ray rate, the upwards drift in the gamma PSD band for basement C2.5 and basement C4 data suggests that pileup with the high-rate 511-keV gamma-rays is

resulting in higher PSD values for most pulses. Note that the basement C11 data was collected in between the basement C2.5 and basement C4 data collection periods, indicating that the upwards drift in PSD values should not be due to hardware drifts.

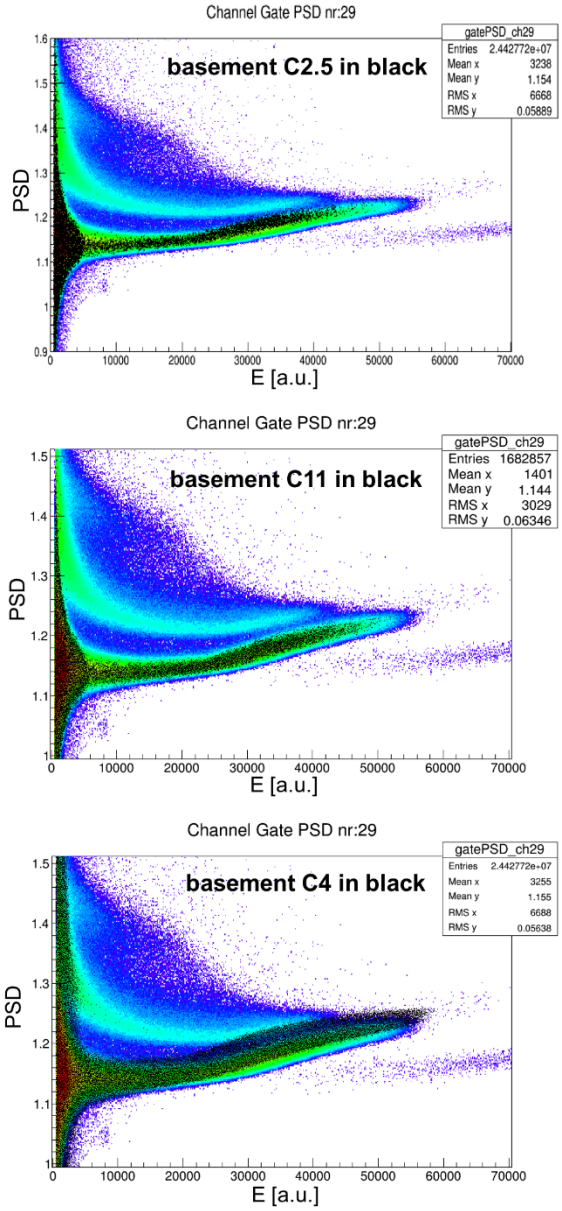

Figure 64: Comparison of the PSD vs. deposited energy E (in arbitrary "adc" units) between the beamline 8 data and all the measured basement locations (superimposed in black) for one NSC channel example. The upwards drift in the gamma PSD band for basement C2.5 and basement C4 data suggests high pile-up rates.

Even though a PSD neutron-gamma boundary is calculated for each separate dataset, we found that the gamma-ray pileup might be creating "fake" PSD-selected neutron events. Figure 65 shows the "time-to-trigger" histograms of the PSD-selected neutron events. The left plot corresponds to a first data collection period at basement C4, or "period I", whose beam power level are shown in Figure 62. The right plot

corresponds to a second data collection period at basement C4, or "period II", and the corresponding beam power level are shown in Figure 63. For both periods, Time-to-Trigger histograms are created for each nominal beam power level (high, medium, low and off) and are normalized by the number of beam pulses in each dataset. Thus, the vertical axis is given in neutrons per pulse.

As can be seen in both plots, the PSD-selected neutron rates strongly depend on the nominal beam power level, even during the time window anti-coincident with the beam pulse. We believe that the intense gamma-ray rate at this location, which depends on the beam power level during the beam operation periods, are piling up and creating "fake" neutron pulses that pass our PSD neutron selection. Figure 66 shows the same histograms of Figure 65, but zoomed down to few microseconds. The spike in rate at ~2 μs for all the beam-on datasets represent the beam-related neutrons during the 1.3-μs prompt window.

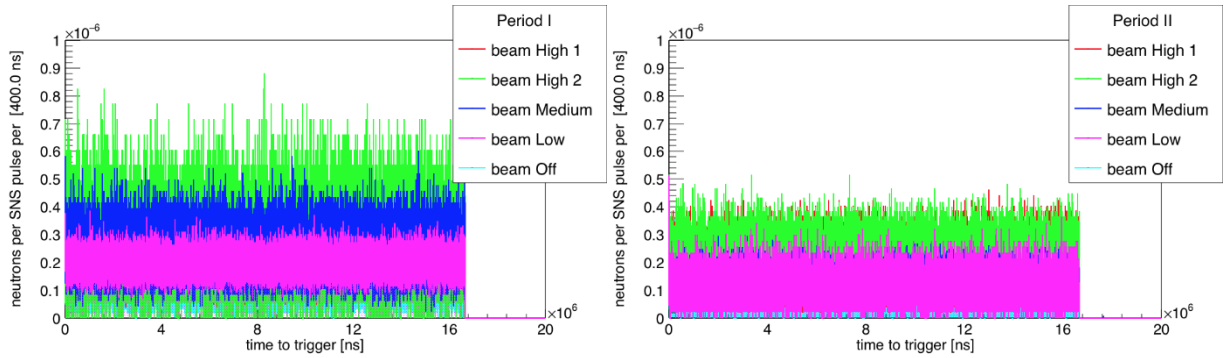

Figure 65: "Time-to-Trigger" histograms of the arrival times of PSD-selected neutron events with respect to the SNS beam signal. The data has been separated in two periods for clarity. The PSD-selected neutron rates strongly depends on the nominal beam power level, which are those represented in Figure 62 and Figure 63.

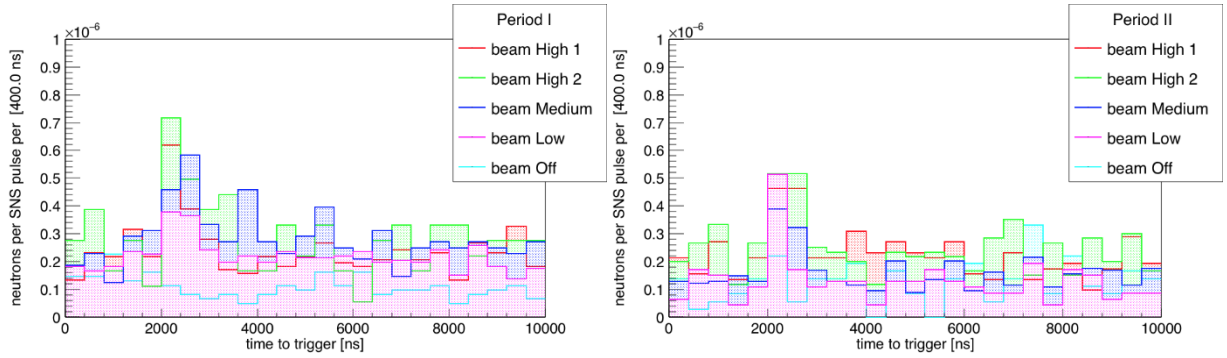

Figure 66: Same "Time-to-Trigger" histograms of Figure 65 zoomed down to few microseconds. The beam-related neutrons are evident as a rate spike at ~2 μs in all the beam-on datasets.

4.2.2.6. Verification with DT Neutron Generator

As a demonstration of the NSC imaging and spectroscopic capabilities, data was collected with a DT Neutron Generator producing an isotropic flux of 14 MeV neutrons. This measurement was done at beamline 14a, during the October 2013 beam off period. Thus, this measurement also served as a check of NSC operation after being transported from SNL, Livermore, to the SNS. Data was collected with the DT generator in front and behind the NSC, as shown in the diagram of Figure 67.

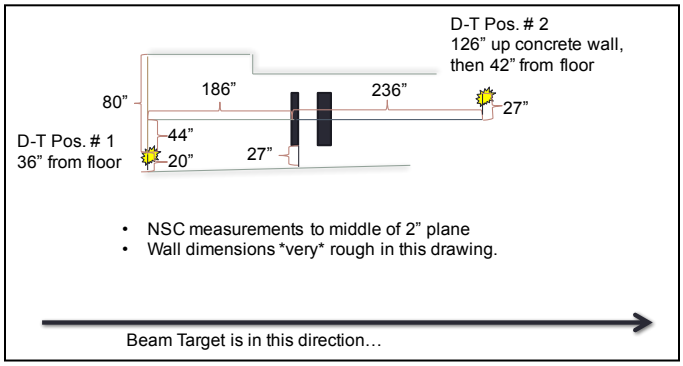

Figure 67: Diagram showing the positioning at beamline 14a of the DT neutron Generator, shown as yellow flashes, with respect to the NSC planes, shown as black rectangles.

The reconstructed spectra, shown in Figure 68, peak at 14 MeV and show the spread due to the poor NSC energy resolution, as discussed in section 4.1. For each DT generator position, the spectra were generated from pairs where: the first event is in the front (thin cells) plane and second in the back (thick cells) plane, the first event is in the back plane and second in the front plane, each event is in a different plane, and finally, events are in any plane. As shown in Figure 68, the spectra for each case is as expected according to the DT generator position. It is interesting to notice that the beamline 14a concrete walls create a cave that reflect the DT generator neutrons back to the NSC when the generator is in position 1, shown by the blue spectra in the left plot of Figure 68, and by the wider spread in the spectra. The resulting backscatter images, shown in Figure 69, also peak at the corresponding DT generator angular direction for each measurement position. The image of position 1 shows the reflecting beamline 14a "cave".

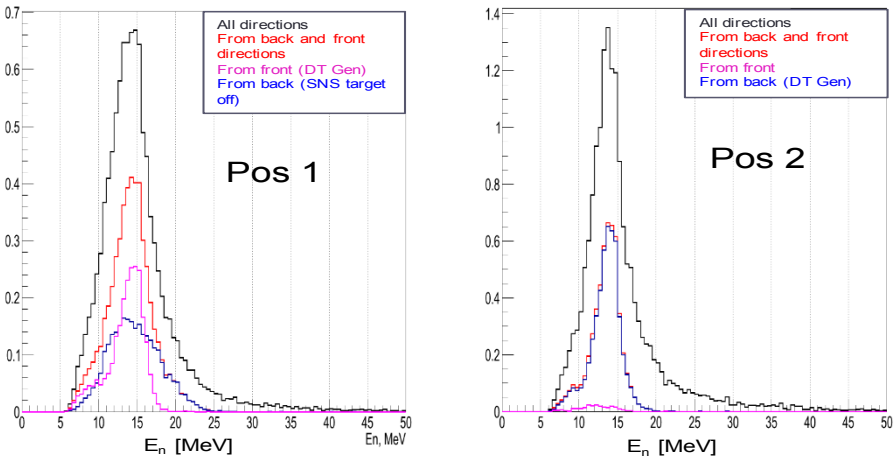

Figure 68: Reconstructed Spectra peak at 14 MeV. For each DT generator position, the spectra were generated from pairs where: (pink) first event is in front plane and second in back plane, (blue) first event is in front plane and second in back plane, (red) each event is in a different plane, (black) events are in any plane.

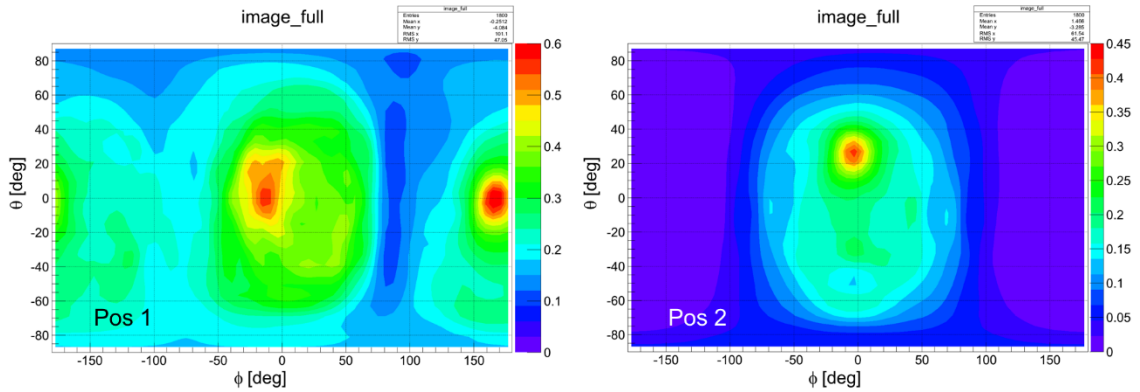

Figure 69: The backscatter images peak at the angular direction corresponding to each DT generator measurement position. In this images, direction (0,0) has been inverted to be at the NSC back. The image of position 1 shows the reflecting beamline 14a "cave" near (0,0).

4.2.2. Results

The main goal of the NSC measurement campaign at SNS has been to characterize the neutron background at the various available SNS locations in order to select the location (or locations) that would allow a successful CNNS experiment. The reconstructed neutron spectra of all measured locations during the 1.3-μs prompt beam window are presented in the left panel of Figure 70. The spectra have been normalized by the total live time of each dataset—equal to the window time duration multiplied by the number of beam pulses during the dataset—and also divided by the energy bin width, and thus are given in "neutron events per [MeV· 'live' second]". The basement C4 location shows the smallest beam-related neutron background, at a rate of $< 10^{-3}$ neutrons/MeV·second in the prompt beam window.

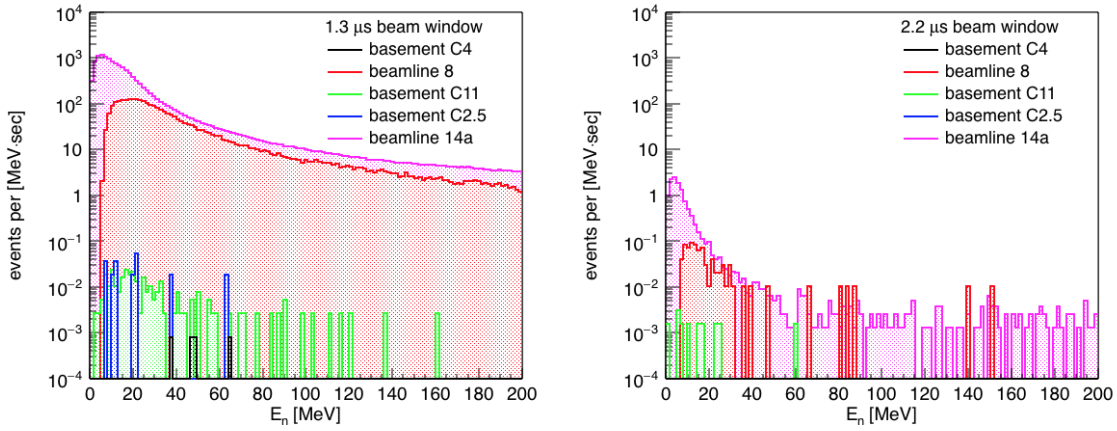

Figure 70: Reconstructed neutron spectra normalized by each dataset lifetime. Left: spectra collected during the 1.3-μs prompt beam window. Right: spectra collected during the 2.2-μs delayed beam window.

The spectra corresponding to the 2.2-μs delayed beam window are presented in the right panel of Figure 70, and show a significant rate reduction and energy softening compared to the 1.3-μs window spectra for all locations. In particular, there were not NSC pair events recorded in the delayed beam window at basement C2.5 and C4. It is important to emphasize that the spectra of Figure 70 have not been adjusted by the NSC efficiency, either angular or spectral efficiency, and thus, are not the absolute (unfolded) neutron rates at the measured locations. As explained in section 4.1, unfolding of the intermediate energy neutron flux from the NSC measured rates is a challenging task that did not fit in the scope of this project. Nevertheless, these background measurements have shown the high suppression of basement C4 beam-related background relative to all other SNS locations and support its choice as the deployment location for the planned Ge detection system.

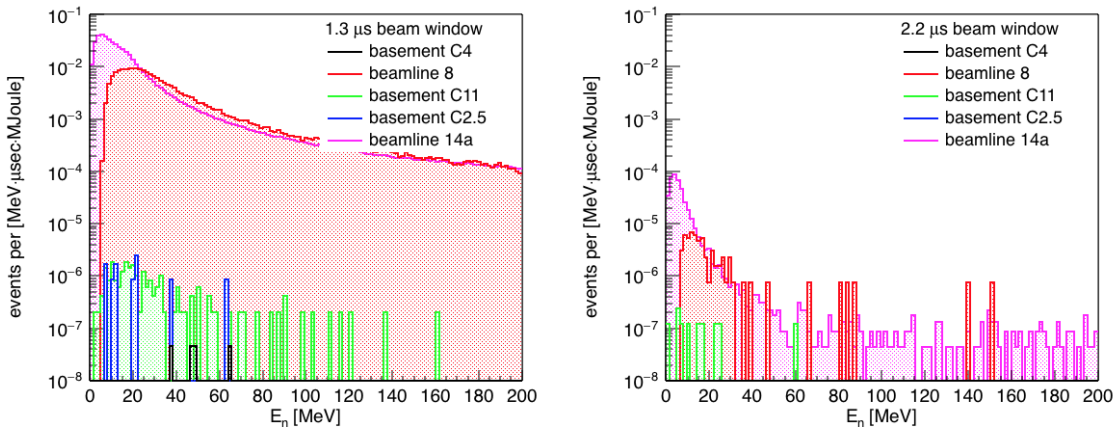

Figure 71: Reconstructed neutron spectra normalized by each dataset total beam power and divided by the window time width in μs. Left: spectra collected during the 1.3-μs prompt beam window. Right: spectra collected during the 2.2-μs delayed beam window.

Figure 71 similarly shows the reconstructed neutron spectra but normalized by the total beam power for each dataset. The histograms have also been divided by the corresponding window time width in μs and the energy bin width, and thus are given in "neutron events per [MeV· μs · MJoule]". Finally, the steady-state neutron background spectra are shown in Figure 72. Since cosmic neutrons represent the main steady-state background source, this rates correspond with the respective location's overburden.

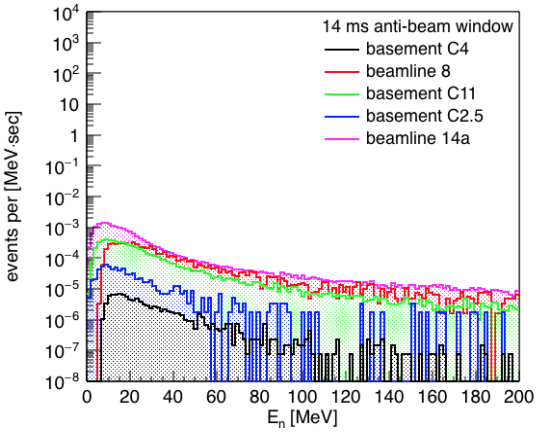

Figure 72: Reconstructed steady-state neutron spectra for all the measured SNS locations. A 14-ms window, anti-coincident with the beam pulse, has been used.

Due to the length of the measurement campaign and the amount of processed data, there were variations in the deposited energy thresholds applied to the different datasets (in hardware and in analysis). For example, a higher threshold applied to the beamline 8 data set removed not only low reconstructed-energy events but possibly reduced the event count for higher energies. Though a uniform threshold would be the ideal, the goals and conclusions of this work have not been affected by those differences in data acquisition and processing.

5. CONCLUSIONS

Existing low mass front end (LMFE) electronics for p-type point (PPC) contact high purity germanium (HPGe) detectors were improved to their limit of sub 100 eV-FWHM in this work. Vibration-free mechanical cooling down to 8 K was demonstrated with a Gifford-McMahon (GM) cycle modified optical cryostat, employing an atmospheric pressure helium heat transfer gas. An off the shelf preamplifier-on-a-chip fabricated in a complementary metal oxide semiconductor (CMOS) application specific integrated circuit (ASIC), originally developed for silicon drift detectors (SDD) formed the basis of the 40 K readout of PPC detectors in this project. Wirebonding to a <1 mm point contact proved to be a robust connection strategy and helped lower the overall noise to 39 eV-FWHM at 43 K. This level of electronic noise demonstrates the ability to operate with an energy threshold below 100 eV. Additional ASIC developments with Brookhaven National Laboratory (BNL) will prove advantageous to lowering the energy threshold, lowering the radioactive background, and increasing the detection efficiency for reactor antineutrinos through the coherent elastic neutrino nuclear scattering process.

For three years, the Neutron Scatter Camera collected extensive data in five different SNS locations in order to select the one with sufficient low background to allow a successful first-time measurement of the CNNS process. An SNS basement location, labeled as C4, shows the smallest measured beam-related neutron background, at a rate of $< 10^{-3}$ neutrons/MeV·second in the 1.3-μs prompt beam window. This location, shielded by a high-density concrete monolith from the mercury target, is also the closest location to the SNS target that is available for the COHERENT experiment. Thus, the C4 location has been selected by the COHERENT collaboration as the likely deployment site for several kilograms of HPGe with the goal to measure and characterize the CNNS process.

6. REFERENCES

1. C. E. Aalseth et al. “Results from a Search for Light-Mass Dark Matter with a P-type Point Contact Germanium Detector”, by CoGeNT Collaboration. Phys.Rev.Lett. 106 (2011) 131301, e-print: arXiv:1002.4703 [astro-ph.CO]
2. S. Agostinelli and et al., "Geant4—A Simulation Toolkit," *Nuclear Instruments and Methods in Physics Research A,* vol. 506, no. 3, pp. 250-303, 2003.
3. Evaluated Nuclear Data File, http://www.nndc.bnl.gov/exfor/endf00.jsp
4. Joint Evaluated Fission and Fusion File, https://www.oecd-nea.org/dbforms/data/eva/evatapes/jeff_31/
5. P. S. Barbeau, J. I. Collar and O. Tench “Large-mass ultralow noise germanium detectors: performance and applications in neutrino and astroparticle physics”, Journal of Cosmology and Astroparticle Physics, vol. 009, 2007.
6. D. Reyna, “A simple parameterization of the cosmic-ray muon momentum spectra at the surface as a function of zenith angle”, arXiv:hep-ph/0604145.
7. Cosmic-ray Shower Library (CRY), http://nuclear.llnl.gov/simulation/main.html
8. D. Akimov et al., “The COHERENT Experiment at the Spallation Neutron Source”, COHERENT Collaboration, e-print: arXiv:1509.08702
9. J. F. Ziegler, “Terrestrial Cosmic Rays,”, IBM J. Res. Develop., vol. 40, No. 1, 1996.
10. N. Mascarenhas, J. Brennan, K. Krenz, P. Marleau, S. Mrowka, “Results with the Neutron Scatter Camera,” IEEE Trans. Nulc. Sci., Col. 56, No. 3, 2009
11. Eljen Technology," [Online]. Available: http://www.eljentechnology.com/images/stories/Data_Sheets/Liquid_Scintillators/EJ309 data sheet.pdf
12. "Struck Innovative Systeme," [Online]. Available: http://www.struck.de/sis3316.html.
13. C. Patrignani et al. (Particle Data Group), Chin. Phys. C, 40, 100001 (2016).
14. Data provided by M. Gerling, Sandia National Laboratories.
15. M. Takada, K. Yajima, H. Yasuda and T. Nakamura, "Simulated neutron response functions of phoswich-type neutron detector and thin organic liquid scintillator," *Progress in Nuclear Science and Technology,* vol. 2, pp. 274-279, 2011.
16. A. Enqvist, C. C. Lawrence, B. M. Wieger, S. A. Pozzi and T. N. Massey, "Neutron light output response and resolution functions in EJ-309 liquid scintillator detectors," *Nuclear Instruments and Methods in Physics Research A,* vol. 715, pp. 79-86, 2013
17. A. C. Kaplan, M. Flaska, A. Enqvist, J. L. Dolan and S. A. Pozzi, "EJ-309 pulse shape discrimination performance with a high gamma-ray-to-neutron ratio and low threshold.," *Nuclear Instruments and Methods in Physics Research A,* vol. 729, pp. 463-468, 2013.
18. M. Moszynski, G. J. Costa, G. Guillaume, B. Heusch, A. Huck, S. Mouatassim, Y. El-Masri, P. Laleu, P. Lipnik, I. Tilquin, F. Hanappe, G. Bizard, D. Durand, J. Peter and B. Tamain, "Identification of different reaction channels of high energy neutrons in liquid scintillators by the pulse shape discrimination method," *Nuclear Instruments and Methods in Physics Research A,* vol. 343, pp. 563-572, 1994.

19. R. S. Onge, A. Galonsky, R. K. Jolly and T. M. Amos, "Organic-scintillator pulse-shape discriminator signtures associated with high-energy neutrons," *Muclear Instruments and Methods,* vol. 126, pp. 391-395, 1975.
20. M. Monterial, P. Marleau, S. Clarke and S. Pozzi, "Application of Bayes' theorem for pulse shape discrimination," *Nuclear Instruments and Methods in Physics Research A,* vol. 795, pp. 318-324, 2015
21. K. A. A. Gamagea, M. J. Joycea and N. P. Hawkesb, "A comparison of four different digital algorithms for pulse-shape discrimination in fast scintillators," *Nuclear Instruments and Methods in Physics Research Section A,* vol. 642, no. 1, pp. 78-83, 2011.
22. L. A. Shepp and Y. Vardi, "Maximum Likelihood Reconstruction for Emission Tomography," *IEEE Transactions on Medical Imaging,* vol. 1, no. 2, pp. 113-122, 1982.
23. Berger, M.J., Coursey, J.S., Zucker, M.A., and Chang, J. (2005), *ESTAR, PSTAR, and ASTAR: Computer Programs for Calculating Stopping-Power and Range Tables for Electrons, Protons, and Helium Ions* (version 1.2.3). [Online] Available: http://physics.nist.gov/Star [2017, 05]. National Institute of Standards and Technology, Gaithersburg, MD.
24. Z. Kohley, E. Lunderberg, P. A. DeYoung, B. T. Roeder, T. Baumann, G. Christian, S. Mosby, J. K. Smith, J. Snyder, A. Spyrou and M. Thoennessen, "Modeling interactions of intermediate-energy neutrons in a plastic scintillator array with Geant4," *Nuclear Instruments and Methods in Physics Research A,* vol. 682, pp. 59-65, 201
25. J. Brennan, R. Cooper, M. Gerling, P. Marleau, N. Mascarenhas and S. Mrowka, "Applying the neutron scatter camera to treaty verification and warhead monitoring," in *IEEE Nuclear Science Symposium Conference Record*, Knoxville, TN, 2010
26. M. Zhang, B. D. Peng, L. Sheng, K. N. Li, X. P. Zhang, Y. Li, B. K. Li, Y. Yuan, P. W. Wang, X. D. Zhang and C. H. Li, "Research of the system response of neutron double scatter imaging for MLEM reconstruction," *Nuclear Instruments and Methods in Physics Research A,* vol. 775, pp. 132-138, 2015

DISTRIBUTION

1 Lawrence Berkeley National Laboratory
Attn: Paul Barton
Applied Nuclear Physics Program
Building 50C, MS50C3396
1 Cyclotron Road, Berkeley, CA 94720

1	MS 9004	Wen L. Hsu	8720	(electronic copy)
1	MS 9004	James C. Lund	8130	(electronic copy)
1	MS 9402	Alfredo M. Morales	8726	(electronic copy)
1	MS 9402	Kristin L. Hertz	8727	(electronic copy)
1	MS 9406	David Reyna	8727	(electronic copy)
1	MS 9402	Mark Gerling	8727	(electronic copy)
1	MS 9406	Belkis Cabrera-Palmer	8727	(electronic copy)
1	MS0899	Technical Library	9536	(electronic copy)


Sandia National Laboratories